Composite Structures 245 (2020) 112344

Contents lists available at ScienceDirect

Composite Structures

journal homepage: www.elsevier.com/locate/compstruct

Adaptive importance sampling based neural network framework for reliability and sensitivity prediction for variable stiffness composite laminates with hybrid uncertainties

Tittu Varghese Mathew[a], P. Prajith[a], R.O. Ruiz[b], E. Atroshchenko[c], S. Natarajan[a,*]

[a] Integrated Modelling and Simulation Lab, Department of Mechanical Engineering, Indian Institute of Technology Madras, Chennai 600036, India
[b] Department of Civil Engineering, Universidad de Chile, Av. Blanco Encalada 2002, Santiago, Chile
[c] School of Civil and Environmental Engineering, University of New South Wales, Sydney, Australia

ARTICLE INFO

Keywords:
Adaptive importance sampling
Artificial neural network
Global reliability sensitivity analysis
Monte Carlo simulations
Probability of failure
Second order reliability method
Variable stiffness composites

ABSTRACT

In this work, we propose to leverage the advantages of both the Artificial Neural Network (ANN) based Second Order Reliability Method (SORM) and Importance sampling to yield an Adaptive Importance Sampling based ANN, with specific application towards failure probability and sensitivity estimates of Variable Stiffness Composite Laminate (VSCL) plates, in the presence of multiple independent geometric and material uncertainties. The performance function for the case studies is defined based on the fundamental frequency of the VSCL plate. The accuracy in both the reliability estimates and sensitivity studies using the proposed method were found to be in close agreement with that obtained using the ANN based brute-force Monte Carlo Simulations (MCS) method, with a significant computational savings of 95%. Moreover, the importance of taking into account the randomness in ply thickness for failure probability estimates is also highlighted quantitatively under the sensitivity studies section.

1. Introduction

Composite materials belong to a class of advanced materials that is made up of two or more chemically and physically different phases separated by an interface. Due to their high strength–to–weight ratio and ease of customization for various requirements, they have been widely used in aerospace industries since the dawn of flight. However, thanks to the inherent statistical nature of material properties of the constituents and the unavoidable fabrication inaccuracies in ply layup and fiber placements, none of the its performance parameters are deterministic in nature.

Composite materials are used extensively both in primary as well as secondary structures of aerospace and mechanical structures. During the course of a product lifetime, such components are exposed to harsh environments, including mechanical vibration. They are found to exhibit superior strength-to-weight and strength-to-stiffness ratios. Since composites are an amalgamation of two or more constituent materials, its effective properties are governed by its material mechanical properties, its density, the stacking sequence and thickness of each ply, orientation angle and so on.

All the above mentioned parameters are not exempt of uncertainties, mainly due to the stochasticity of the material constituents and the unavoidable fabrication inaccuracies in ply layout and fiber placements. In this context, the uncertainty associated to model parameters is understood as incomplete information, facilitating their probabilistic description grounded in the information theory. Hence, all such mechanical and geometric uncertainties must be quantified and taken into account for probabilistic prediction of composite structure response. Natural frequencies of components within safety critical assemblies often tend to be so close to each other, that a small uncertainty in the effective characteristics of any of its components can have a catastrophic effect on the overall system performance. Therefore, we must be able to quantify the uncertainty (at least in its first fundamental frequency) of a critical component made of composites, and as a by-product predict its failure reliability based on a set user-defined criteria. It is also critical to perform a detailed sensitivity study of laminate behaviour to the uncertainty in each input, modeled here as random parameters.

Laminated fibre-reinforced composites [1,2] are made up of straight and unidirectional fibers that are homogeneously distributed in each lamina. For such materials, from a macroscopic sense, it is safe to consider that its stiffness does not vary at the laminate level. However,

* Corresponding author at: Department of Mechanical Engineering, Indian Institute of Technology Madras, Chennai 600036 India.
E-mail address: snatarajan@iitm.ac.in (S. Natarajan).

https://doi.org/10.1016/j.compstruct.2020.112344
Received 24 November 2019; Received in revised form 20 March 2020; Accepted 6 April 2020
Available online 13 April 2020
0263-8223/

from the early nineties, a shift in the general trend in composite manufacturing has been observed, where the stiffness is purposely made to vary within a lamina, which supposedly lead to more efficient designs [3,4]. There exists several ways to achieve Variable Stiffness Composite Laminates (VSCL). A few among them are by using curvilinear fibers [5–7], by varying the volume fraction of fibers [8,9], or by adding and dropping plies to the laminates [10,11]. There exists a few advantages for going with variable fibre orientation over others, such as, continuous variation of the stiffness with membrane coordinates and avoiding abrupt changes in the thickness which may lead to stress concentrations, as reported in Ribeiro et al. [12]. One other reason that complements the increasing availability of curved fibre laminates is the capability of present tow-placement machines to control the fibre tow placement individually.

The study of static and free vibration response of VSCL plates have received considerable attention. The natural modes of VSCL plates with curvilinear fibers using the *p*-version finite element, that follows a third order deformation theory, was examined in [13]. Geometric non-linear vibration studies of VSCL plates was studied using the first order shear deformation theory (FSDT) in [14]. The dynamic instability of VSCL plates using the Rayleigh–Ritz method was studied in [15]. Anand et al., [16] studied the free vibration characteristics of VSCL plates using a higher order accurate theory. The influence of environmental effects and geometric discontinuities were also considered. All the aforementioned studies assumed that the geometry and the material parameters were deterministic.

Numerical investigation of the stochastic vibration behaviour of Constant Stiffness Composite Laminate (CSCL) have been studied in [17–19]. A mean-centered second-moment method to study the free vibration and reliability study of composite cantilevers was done in [20]. A stochastic finite element method for the analysis of composite plates was proposed in [17]. A First Order Reliability Method (FORM) to study shear deformable laminated composite plates was used in [21]. For more details, interested readers are referred to a comprehensive review on the reliability studies of composite structures and references therein.

Monte Carlo Simulations (MCS) are another brute-force method for reliability analysis, given a large sample size and at the expense of considerable computational time to achieve a reasonable accuracy. Shaker et al. [22] was one of the first in using FORM and Second Order Reliability Method (SORM) for reliability analysis of composite plates under free vibration using the stochastic finite element method. However, the uncertainties in that study were limited to only laminae stiffness properties, material density and ply orientation angles. The SORM has been proven to be a superior tool over the MCS for stochastic analysis of free vibrating composite plates. But, one of the major drawbacks of the SORM is that it requires the second order derivative of the performance function w.r.t each of the random parameters in the system. This limitation could be partially circumvented using a symbolic solver. However, such a circumvention can become obsolete when the derivative of the performance function w.r.t the random parameters like the ply thickness are required. [23] showed the importance of considering uncertainty in the ply thickness for reliability analysis of fiber-reinforced composites under multi-axial loads.

Structural reliability analysis using Artificial Neural Network (ANN) has been in the mainstream research since past two decades. Hurtado [24] gave a comprehensive overview on the use of neural networks in stochastic mechanics. ANN has been successfully used in the structural reliability and optimization studies in the past [25–30]. The art of combining ANN with reliability methods like FORM, SORM or MCS is termed as "Neural Network based Reliability". A comparison of ANN against other reliability methods was done in [31], wherein a significant reduction in computational time was reported. A comparative study between Multi-Layer Perceptron (MLP) and Radial-Basis Function (RBF) based Neural Network architecture in replacing the FEM in the probabilistic analysis of structures was provided in [24]. A new, higher order neuron was developed for the deep neural network model to improve its prediction performance for the compressive strength of foamed concrete, another form of composite material, in [32]. [33,34] substituted FEM with a trained neural network to perform reliability studies on composite plates under static loading.

However, to the best of knowledge of the authors, there exists very few literature that deals with the reliability studies of VSCL plates using FORM/SORM/MCS. Sohouli et al. [35] presented a detailed reliability study on the VSCL plate structures using two different limit state function definition, one based on the tip deflection and the other based on the first-ply failure criterion by means of Tsai-Wu criterion. However, only uncertainties in the material were taken into account and the analysis was being limited to only static concentrated/distributed load cases. In the present work, the advantage of both the neural network and the adaptive importance sampling in better approximating the performance function at the Maximum Probability of failure Point (MPP) are exploited to predict the failure probability of VSCL w.r.t its first mode of free vibration, while taking into account both material and geometric uncertainties. An MLP-based neural network architecture is used to obtain an ANN-derived function between the input random parameters and the output limit state function values.

The paper is organized as follows. Section 2 presents the finite element formulation for the free vibration studies of a VSCL plate were cutouts are modelled using eXtended Finite Element Method (XFEM). Section 3 introduces the reader to the basics of both First Order and Second Order based Reliability Methods and highlight certain limitations in its applications pertaining to the chosen case study using VSCL plates. ANN based surrogate modelling is introduced in Section 4 along with its architecture terminology and the procedure to derive first and second order derivatives of ANN approximated functions. After a short exposition on its extension for deriving FORM/SORM estimates using trained metamodel in Section 5, Section 6 discusses about the two main methods adopted for sampling design points for training data, namely the brute-force MCS and the importance sampling. Section 7 concludes the theoretical discussions where global reliability based sensitivity analysis procedure is discussed using ANN trained metamodel using two different approaches. Finally, Section 8 puts all the theoretical formulations into practice using the case study of VSCL plates with a set of carefully chosen random input parameters and their distributions taken mostly from literature. The main take-away points from this work are summarised in Section 9.

2. Theoretical formulation of a VSCL plate

The First-order Shear Deformation Theory (FSDT), developed by Reissner and Mindlin for thin and moderately thick plates assumes that there exists a linear variation of the displacement through the thickness of the plate and that the thickness does not change during the deformation. To illustrate the energy formulation for a VSCL plate, a rectangular plate with an elliptic cutout is used, as shown in Figure 1.

The plate dimensions are taken as: length a along the x axis, width b along the y axis and thickness h along the z axis. The geometry of the elliptical cutout is represented using the major axis d and the minor axis c. The field displacements using the FSDT theory can be expressed as functions of the mid-plane displacements u_0, v_0, w_0 and rotations β_x and β_y of x-axis and y-axis of the plate respectively as follows:

$$\begin{aligned} u(x, y, z) &= u_0(x, y, t) + z\beta_x(x, y, t) \\ v(x, y, z, t) &= v_0(x, y, t) + z\beta_y(x, y, t) \\ w(x, y, z, t) &= w_0(x, y, t) \end{aligned} \tag{1}$$

where t is the time. The linear strain–displacement relationship is given by:

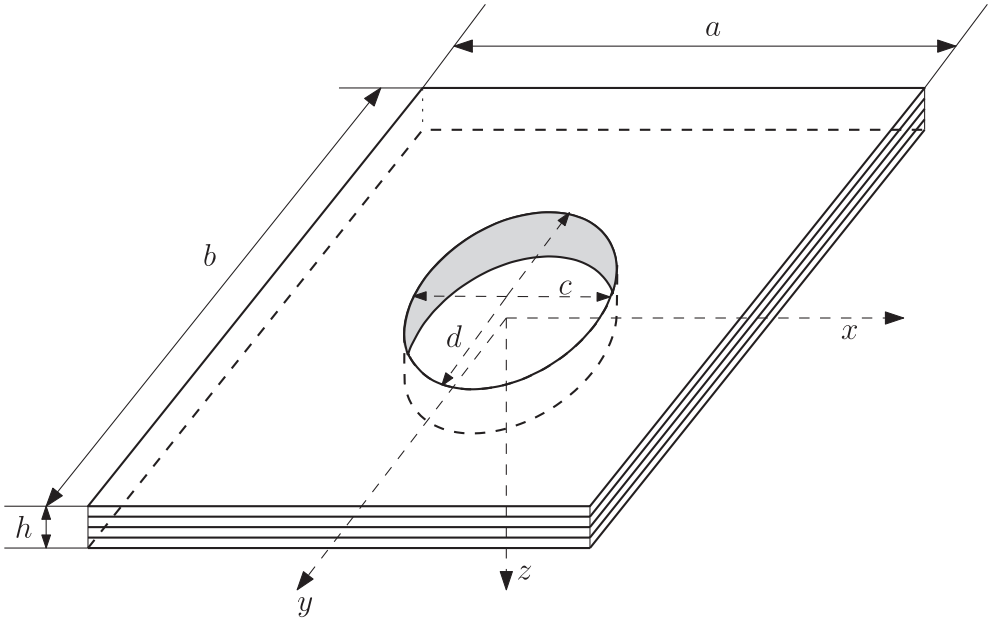

Fig. 1. Composite Laminate plate with an elliptic hole. Cartesian coordinates are shown as $x - y - z$.

$$\varepsilon = \begin{Bmatrix} \varepsilon_{xx} \\ \varepsilon_{yy} \\ 2\varepsilon_{xy} \\ 2\varepsilon_{xz} \\ 2\varepsilon_{yz} \end{Bmatrix} = \begin{Bmatrix} \frac{\partial u_0}{\partial x} \\ \frac{\partial v_0}{\partial y} \\ \frac{\partial u_0}{\partial y} + \frac{\partial v_0}{\partial x} \\ \frac{\partial w_0}{\partial x} + \beta_x \\ \frac{\partial w_0}{\partial y} + \beta_y \end{Bmatrix} + z \begin{Bmatrix} \frac{\partial \beta_x}{\partial x} \\ \frac{\partial \beta_y}{\partial y} \\ \frac{\partial \beta_x}{\partial y} + \frac{\partial \beta_y}{\partial x} \\ 0 \\ 0 \end{Bmatrix} \tag{2}$$

The above strain-displacement relation can be rewritten as follows:

$$\varepsilon = \begin{Bmatrix} \varepsilon_p \\ \mathbf{0} \end{Bmatrix} + \begin{Bmatrix} z\varepsilon_b \\ \varepsilon_s \end{Bmatrix} \tag{3}$$

where

$$\varepsilon_p = \begin{Bmatrix} u_{0,x} \\ v_{0,y} \\ u_{0,y} + v_{0,x} \end{Bmatrix}, \ \varepsilon_b = \begin{Bmatrix} \beta_{x,x} \\ \beta_{y,y} \\ \beta_{x,y} + \beta_{y,x} \end{Bmatrix}, \ \varepsilon_s = \begin{Bmatrix} \beta_x + w_{0,x} \\ \beta_y + w_{0,y} \end{Bmatrix} \tag{4}$$

where ε_p, ε_b and ε_s are the mid-plain strain, bending strain and shear strain. The subscript 'comma' represents the partial derivative w.r.t the spatial coordinate that succeeds it. The membrane stress resultants **N** and the bending stress resultants **M** can be related to the membrane strain ε_p and bending strain ε_b through the following relation [36]:

$$\begin{aligned} \mathbf{N} &= \begin{Bmatrix} N_{xx} \\ N_{yy} \\ N_{xy} \end{Bmatrix} = \mathbf{A}\varepsilon_p + \mathbf{B}\varepsilon_b \\ \mathbf{M} &= \begin{Bmatrix} M_{xx} \\ M_{yy} \\ M_{xy} \end{Bmatrix} = \mathbf{B}\varepsilon_p + \mathbf{D}_b\varepsilon_b \end{aligned} \tag{5}$$

where the matrices $\mathbf{A}= A_{ij}$, $\mathbf{B}= B_{ij}$ and $\mathbf{D}_b = D_{ij}$ (i,j = 1,2,6) are the extensional, bending-extensional and bending stiffness coefficients defined as:

$$\left\{A_{ij}, B_{ij}, D_{ij}\right\} = \int_{-h/2}^{h/2} \overline{Q}_{ij} \left\{1, z, z^2\right\} dz \tag{6}$$

Similarly, the transverse shear force $\mathbf{Q}= \{Q_{xz}, Q_{yz}\}$ is related to the transverse shear strain ε_s as follows:

$$\begin{aligned} Q_{xz} &= K_s \int_{-h/2}^{h/2} \sigma_{xz} dz = K_s \overline{Q}_{55}(\beta_x + w_{0,x}) \\ Q_{yz} &= K_s \int_{-h/2}^{h/2} \sigma_{yz} dz = K_s \overline{Q}_{44}(\beta_y + w_{0,y}) \end{aligned} \tag{7}$$

where K_s is the shear correction factor. The global stiffness coefficients $\overline{Q}_{ij}$ are derived from the local stiffness coefficients Q_{ij} defined along the local coordinate system that aligns along with the fiber. The local stiffness matrices Q_{ij} are defined as follows:

$$Q_{11} = \frac{E_1}{1 - \nu_{12}\nu_{21}}, \ Q_{22} = \frac{E_2}{1 - \nu_{12}\nu_{21}}, \ Q_{12} = Q_{21} = \frac{\nu_{12}E_2}{1 - \nu_{12}\nu_{21}}, \ Q_{16} = Q_{26} = 0 \tag{8}$$

$$Q_{44} = G_{23}, \ Q_{55} = G_{13}, \ Q_{66} = G_{12} \tag{9}$$

where the subscript '1' refers to the local material direction (fiber direction), '2' refers to that direction perpendicular to the local fiber direction and lying within the plane of ply '12'. With the help of a coordinate transformation matrix, the local stiffness coefficients can be transformed to its global stiffness coefficients. However, the curvilinear fibre laminates differ from straight fibre laminates, in the fact that the orientation of the principal material axis does not remain constant in the lamina domain. This means that the transformed stiffness coefficient matrix $\overline{\mathbf{Q}}$ doesn't remain constant and become function of spatial x direction. For example, the first element of matrix, namely $\overline{Q}_{11}$ is:

$$\overline{Q}_{11} = Q_{11}c(x)^4 + 2(Q_{12} + 2Q_{33})c(x)^2 s(x)^2 + Q_{12}s(x)^4 \tag{10}$$

where $c(x) = cos(\theta(x))$ and $s(x) = sin(\theta(x))$ in which $\theta(x)$ is the fibre orientation angle of the VSCL plate, measured from the x axis of the plate to the fibre axis angle at position x. In this study, it is assumed that the fibre path variation is represented as follows:

$$\theta(x) = \frac{2(\Theta_0 - \Theta_1)}{a}\left|x\right| + \Theta_0 \tag{11}$$

where Θ_0 is the angle between the fibre and the x axis at $x = 0$ and Θ_1 is the fibre angle at the panel ends ($x = \pm a/2$). The fibre orientation for the k'th layer is then represented as $<\Theta_0^k|\Theta_1^k>$ as shown in Figure 2. However, due to manufacturing constraints, these sets of fiber ply angles cannot take arbitrary combination of values, as was pointed out by Akhavan et al. [13]. In his seminal work on natural modes of vibration of composite structures with variable fibers, he proposed a relation (c.f.Eq. (12)) wherein for a given set of fiber ply pair $<\Theta_0^k|\Theta_1^k>$ to be

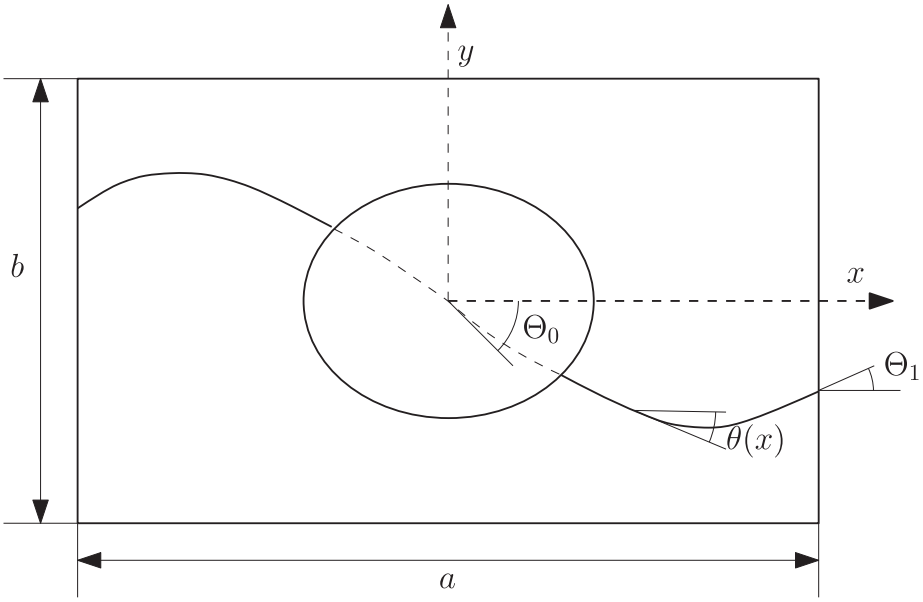

Fig. 2. Curved fiber along with plate dimensions. As shown here, angle Θ_0 has a negative value. Positive value for $\theta(x)$ are defined in the counter-clockwise direction [12].

feasible from a manufacturing perspective, the local curvature of the fiber, $\kappa(x)$, should not exceed a value of 3.28.

$$\kappa(x) = 2\frac{(\Theta_1 - \Theta_0)}{a} cos\left(\left(\Theta_1 - \Theta_0\right)\frac{x}{a/2} + \Theta_0\right) < 3.28 \tag{12}$$

The strain energy function U is then given by:

$$\begin{aligned} U(\delta) &= \frac{1}{2}\int_\Omega \left\{\varepsilon_p^T \mathbf{N} + \varepsilon_b^T \mathbf{M} + \varepsilon_s^T \mathbf{Q}\right\} d\Omega \\ &= \frac{1}{2}\int_\Omega \left\{\varepsilon_p^T \mathbf{A}\varepsilon_p + \varepsilon_p^T \mathbf{B}\varepsilon_b + \varepsilon_b^T \mathbf{B}\varepsilon_p + \varepsilon_b^T \mathbf{D}\varepsilon_b + \varepsilon_s^T \mathbf{E}\varepsilon_s\right\} d\Omega \end{aligned} \tag{13}$$

where $\delta = \{u_0, v_0, w_0, \beta_x, \beta_y\}$ is the vector of degrees of freedom associated to the displacement field in finite element discretization. Following the procedure outlined in [37], the strain energy function $U(\delta)$ can be rewritten as:

$$U(\delta) = \frac{1}{2}\delta^T \mathbf{K}\delta \tag{14}$$

where $\mathbf{K}$ is the linear stiffness matrix. In a similar way, the kinetic energy of the plate is given by:

$$T(\delta) = \frac{1}{2}\int_\Omega \left\{I_0\left(\dot{u}_0^2 + \dot{v}_0^2 + \dot{w}_0^2\right) + I_1\left(\dot{\theta}_x^2 + \dot{\theta}_y^2\right)\right\} d\Omega \tag{15}$$

where $I_0 = \int_{-h/2}^{h/2} \rho dz$ and $I_1 = \int_{-h/2}^{h/2} z^2 \rho dz$, ρ is the mass density. Substituting Eq. (14) and Eq. (15) in a Lagrangian equation of motion, one obtains the following governing equation:

$$\mathbf{M}\ddot{\delta} + \mathbf{K}\delta = 0 \tag{16}$$

where $\mathbf{M}$ is the consistent mass matrix. After substituting the characteristic of the time function $\ddot{\delta} = \omega^2\delta$, following relation is obtained:

$$(\mathbf{K} - \omega^2\mathbf{M})\delta = 0 \tag{17}$$

where ω is the natural frequency.

2.1. Spatial discretization

The plate element employed here is a $\mathscr{C}^o$ continuous shear flexible field consistent element with five degrees of freedom $(u_o, v_o, w_o, \beta_x, \beta_y)$ at four nodes in a 4-noded quadrilateral (QUAD-4) element. The displacement field within the element is approximated by:

$$\left\{u_o^e, v_o^e, w_o^e, \beta_x^e, \beta_y^e\right\} = \sum_{J=1}^{4} N_J \left\{u_{oJ}, v_{oJ}, w_{oJ}, \beta_{xJ}, \beta_{yJ}\right\}, \tag{18}$$

where u_{oJ}, v_{oJ}, w_{oJ}, β_{xJ}, β_{yJ} are the nodal degrees of freedom and N_J are the shape functions for the bi-linear QUAD-4 element. In this study, to alleviate the shear locking phenomenon, field redistributed shape functions [38,39] are employed. The finite element framework requires the underlying finite element mesh to conform to the discontinuity surface. The recent introduction of implicit boundary definition-based methods, viz., the extended/generalized FEM (XFEM/GFEM), alleviates the shortcomings associated with the meshing of the discontinuity surface. In this study, the partition of unity framework is employed to represent the discontinuity surface (cutout geometry) independent of the underlying mesh.

$$\begin{aligned} (u_0^h, v_0^h, w_0^h, \beta_x^h, \beta_y^h)(\mathbf{x}) = &\underbrace{\sum_{I\in\mathscr{N}^{\text{fem}}} N_I(\mathbf{x})(u_0^s, v_0^s, w_0^s, \beta_x^s, \beta_y^s)_I}_{\text{FEM}} \\ &+ \underbrace{\sum_{J\in\mathscr{N}^{\text{c}}} N_J(\mathbf{x})H(\mathbf{x})(b^{u_0}, b^{v_0}, b^{w_0}, b^{\beta_x}, b^{\beta_y})_J}_{\text{Enriched part}} \end{aligned} \tag{19}$$

where $\mathscr{N}^{\text{fem}}$ is a set of all the nodes in the finite element mesh and $\mathscr{N}^{\text{c}}$ is a set of nodes that are enriched with the Heaviside function. In Eq. (19), $\left(u_I^s, v_I^s, w_I^s, \beta_{xI}^s, \beta_{yI}^s\right)$ are the nodal unknown vectors associated with the continuous part of the finite element solution, b_J is the nodal enriched degree of freedom vector associated with the Heaviside (discontinuous) function. In this study, a level set approach is followed to model the cutouts. The geometric interface (for example, the boundary of the cutout) is represented by the zero level curve $\phi \equiv \phi(\mathbf{x}, t) = 0$. The interface is located from the value of the level set information stored at the nodes. The standard FE shape functions can be used to interpolate ϕ at any point $\mathbf{x}$ in the domain as:

$$\phi(\mathbf{x}) = \sum_I N_I(\mathbf{x})\phi_I \tag{20}$$

where the summation is over all the nodes in the connectivity of the elements that contact $\mathbf{x}$ and ϕ_I are the nodal values of the level set function. For circular cutout, the level set function is given by:

$$\phi_I = ||\mathbf{x}_I - \mathbf{x}_c|| - r_c \tag{21}$$

where $\mathbf{x}_c$ and r_c are the center and the radius of the cutout. Based on the level set approach, the Heaviside function $H(\mathbf{x})$ in Eq. (19) becomes:

$$H(\mathbf{x}) = \begin{cases} 0, & \text{if } \phi(\mathbf{x}) < 0 \\ 1, & \text{if } \phi(\mathbf{x}) > 0 \end{cases} \tag{22}$$

2.1.1. Elements of stiffness and mass matrices

In this section, the elements of the stiffness and mass matrices are derived using extended finite element formulation. Substituting Eq. (19) in Eq. (4), one gets the following:

$$\varepsilon_p^h = \sum_{i\in\mathscr{N}^{\text{fem}}} \begin{bmatrix} \frac{\partial N_i}{\partial x} & 0 & 0 & 0 & 0 \\ 0 & \frac{\partial N_i}{\partial y} & 0 & 0 & 0 \\ \frac{\partial N_i}{\partial y} & \frac{\partial N_i}{\partial x} & 0 & 0 & 0 \end{bmatrix} \begin{Bmatrix} u_0^s \\ v_0^s \\ w_0^s \\ \beta_x^s \\ \beta_y^s \end{Bmatrix}_i + \sum_{j\in\mathscr{N}^{\text{c}}} \begin{bmatrix} \widehat{H(\mathbf{x})}\frac{\partial N_j}{\partial x} & 0 & 0 & 0 & 0 \\ 0 & \widehat{H(\mathbf{x})}\frac{\partial N_j}{\partial y} & 0 & 0 & 0 \\ \widehat{H(\mathbf{x})}\frac{\partial N_j}{\partial y} & \widehat{H(\mathbf{x})}\frac{\partial N_j}{\partial x} & 0 & 0 & 0 \end{bmatrix} \begin{Bmatrix} b^{u_0} \\ b^{v_0} \\ b^{w_0} \\ b^{\beta_x} \\ b^{\beta_y} \end{Bmatrix}_j$$

$$\varepsilon_b^h = \sum_{i\in\mathscr{N}^{\text{fem}}} \begin{bmatrix} 0 & 0 & 0 & \frac{\partial N_i}{\partial x} & 0 \\ 0 & 0 & 0 & 0 & \frac{\partial N_i}{\partial y} \\ 0 & 0 & 0 & \frac{\partial N_i}{\partial y} & \frac{\partial N_i}{\partial x} \end{bmatrix} \begin{Bmatrix} u_0^s \\ v_0^s \\ w_0^s \\ \beta_x^s \\ \beta_y^s \end{Bmatrix}_i + \sum_{j\in\mathscr{N}^{\text{c}}} \begin{bmatrix} 0 & 0 & 0 & \widehat{H(\mathbf{x})}\frac{\partial N_j}{\partial x} & 0 \\ 0 & 0 & 0 & 0 & \widehat{H(\mathbf{x})}\frac{\partial N_j}{\partial y} \\ 0 & 0 & 0 & \widehat{H(\mathbf{x})}\frac{\partial N_j}{\partial y} & \widehat{H(\mathbf{x})}\frac{\partial N_j}{\partial x} \end{bmatrix} \begin{Bmatrix} b^{u_0} \\ b^{v_0} \\ b^{w_0} \\ b^{\beta_x} \\ b^{\beta_y} \end{Bmatrix}_j$$

$$\varepsilon_s^h = \sum_{i\in\mathscr{N}^{\text{fem}}} \begin{bmatrix} 0 & 0 & \frac{\partial N_i}{\partial x} & N_i & 0 \\ 0 & 0 & \frac{\partial N_i}{\partial y} & 0 & N_i \end{bmatrix} \begin{Bmatrix} u_0^s \\ v_0^s \\ w_0^s \\ \beta_x^s \\ \beta_y^s \end{Bmatrix}_i + \sum_{j\in\mathscr{N}^{\text{c}}} \begin{bmatrix} 0 & 0 & \widehat{H(\mathbf{x})}\frac{\partial N_j}{\partial x} & \widehat{H(\mathbf{x})}N_j & 0 \\ 0 & 0 & \widehat{H(\mathbf{x})}\frac{\partial N_j}{\partial y} & 0 & \widehat{H(\mathbf{x})}N_j \end{bmatrix} \begin{Bmatrix} b^{u_0} \\ b^{v_0} \\ b^{w_0} \\ b^{\beta_x} \\ b^{\beta_y} \end{Bmatrix}_j$$

where the derivative of the Heaviside function w.r.t the spatial coordinates exists only at the interface location and $\widehat{H(\mathbf{x})} = H(\mathbf{x}) - H(\mathbf{x}_j)$. The above set of equations can be rewritten in the form of their respective strain displacement matrices as follows:

$$\boldsymbol{\varepsilon}_p^h = \mathbb{B}_p^s\boldsymbol{\delta}^s + \mathbb{B}_p^e\boldsymbol{\delta}^e, \quad \boldsymbol{\varepsilon}_b^h = \mathbb{B}_b^s\boldsymbol{\delta}^s + \mathbb{B}_b^e\boldsymbol{\delta}^e, \quad \boldsymbol{\varepsilon}_s^h = \mathbb{B}_s^s\boldsymbol{\delta}^s + \mathbb{B}_s^e\boldsymbol{\delta}^e \tag{23}$$

where $\mathbb{B}_p$, $\mathbb{B}_b$ and $\mathbb{B}_s$ are the membrance, bending and shear strain–-displacement matrices, respectively, the superscripts 's' and 'e' stands for the standard and enriched parts. Substituting Eq. (23) into Eq. (13) and upon further simplification, one gets the following elemental stiffness matrix:

$$\mathbf{K}^e = \begin{bmatrix} \mathbf{K}_{ss}^e & \mathbf{K}_{se}^e \\ \mathbf{K}_{es}^e & \mathbf{K}_{ee}^e \end{bmatrix} \tag{24}$$

where

$$\mathbf{K}_{ss}^e = \int_{\Omega_e} \left\{ \mathbb{B}_p^{s\,T}\mathbf{A}\mathbb{B}_p^s + \mathbb{B}_p^{s\,T}\mathbf{B}\mathbb{B}_b^s + \mathbb{B}_b^{s\,T}\mathbf{B}\mathbb{B}_p^s + \mathbb{B}_b^{s\,T}\mathbf{D}\mathbb{B}_b^s + \mathbb{B}_s^{s\,T}\mathbf{E}\mathbb{B}_s^s \right\} d\Omega$$

$$\mathbf{K}_{se}^e = \int_{\Omega_e} \left\{ \mathbb{B}_p^{s\,T}\mathbf{A}\mathbb{B}_p^e + \mathbb{B}_p^{s\,T}\mathbf{B}\mathbb{B}_b^e + \mathbb{B}_b^{s\,T}\mathbf{B}\mathbb{B}_p^e + \mathbb{B}_b^{s\,T}\mathbf{D}\mathbb{B}_b^e + \mathbb{B}_s^{s\,T}\mathbf{E}\mathbb{B}_s^e \right\} d\Omega$$

$$\mathbf{K}_{es}^e = \int_{\Omega_e} \left\{ \mathbb{B}_p^{e\,T}\mathbf{A}\mathbb{B}_p^s + \mathbb{B}_p^{e\,T}\mathbf{B}\mathbb{B}_b^s + \mathbb{B}_b^{e\,T}\mathbf{B}\mathbb{B}_p^s + \mathbb{B}_b^{e\,T}\mathbf{D}\mathbb{B}_b^s + \mathbb{B}_s^{e\,T}\mathbf{E}\mathbb{B}_s^s \right\} d\Omega$$

$$\mathbf{K}_{ee}^e = \int_{\Omega_e} \left\{ \mathbb{B}_p^{e\,T}\mathbf{A}\mathbb{B}_p^e + \mathbb{B}_p^{e\,T}\mathbf{B}\mathbb{B}_b^e + \mathbb{B}_b^{e\,T}\mathbf{B}\mathbb{B}_p^e + \mathbb{B}_b^{e\,T}\mathbf{D}\mathbb{B}_b^e + \mathbb{B}_s^{e\,T}\mathbf{E}\mathbb{B}_s^e \right\} d\Omega$$

Similarly, Eq. (15) can be written as:

$$T^e = \frac{1}{2} \left\{ \dot{\boldsymbol{\delta}}_s^T, \dot{\boldsymbol{\delta}}_e^T \right\} \mathbf{M}^e \begin{Bmatrix} \dot{\boldsymbol{\delta}}_s \\ \dot{\boldsymbol{\delta}}_e \end{Bmatrix} \tag{25}$$

Substituting Eq. (19) into the above relation, one gets to the element mass matrix as follows:

$$\mathbf{M}^e = \begin{bmatrix} \mathbf{M}_{ss}^e & \mathbf{M}_{se}^e \\ \mathbf{M}_{es}^e & \mathbf{M}_{ee}^e \end{bmatrix} = \begin{bmatrix} \int_{\Omega_e} \mathbf{N}^T\rho\mathbf{N}d\Omega & \int_{\Omega_e} \mathbf{N}^T\rho\Big(H(\mathbf{x})\mathbf{N}\Big)d\Omega \\ \int_{\Omega_e} (H(\mathbf{x})\mathbf{N})^T\rho\mathbf{N}d\Omega & \int_{\Omega_e} (H(\mathbf{x})\mathbf{N})^T\rho\Big(H(\mathbf{x})\mathbf{N}\Big)d\Omega \end{bmatrix} \tag{26}$$

where ρ consists of I_0 and I_1. Figure 3 shows a finite element mesh for a plate with a hole, where both the enriched nodes in the presence of a cutout and constrained nodes are highlighted.

A consequence of adding custom tailored enrichment functions to the FE approximation basis, which are not necessarily smooth functions is that, special care has to be taken in numerically integrating over the elements that are intersected by the discontinuity surface. The standard Gaußquadrature cannot be applied in elements enriched by discontinuous terms, because Gaußquadrature implicitly assumes a polynomial approximation. In the present study, a triangular quadrature with sub-division is employed along with the integration rules described in Table 1. For the elements that are not enriched, a standard 2×2 Gaussian quadrature rule is used.

3. Structural reliability analysis

The analysis and design of complex engineering systems depend heavily on the predictions from numerical models like finite element analysis, while its accuracy depends on how close the digital representation approximates the real-world system. Structural Reliability Analysis (SRA) aims to provide a rational framework to address uncertainties in structural design so that the later can be more objective and less dependent on unrealistic assumptions. The theory behind SRA is formulated around the concept of probability of failure:

$$P_f = Prob\Big[g(\mathbf{x}) \leqslant 0\Big] = \int_{g(\mathbf{x})\leqslant 0} f_X(\mathbf{x})\mathrm{d}\mathbf{x} \tag{27}$$

where $f_X(\mathbf{x})$ is the joint Probability Density Function (PDF) of random vector X and $g(\mathbf{x})$ is the limit state function, where $g(\mathbf{x}) \leqslant 0$ denotes the failure domain and $g(\mathbf{x}) > 0$ is the safe domain. Though the definition in Eq. (27) looks simple, its exact integration through direct integration is often intractable for two reasons: (1) dimension of integral is usually too high in case of multiple input random parameters and (2) the shape of the limit state function $g(\mathbf{x})$ could be complicated with complex topology, specially for low failure probabilities. SRA methods can be broadly classified into three categories: Taylor series-based approaches such as the First Order Reliability analysis Method (FORM) and Second Order Reliability analysis Method (SORM), simulation based methods such as MCS and its variants and surrogate methods such as the Response Surface Method (RSM) and the Kriging meta-model [40]. In the following subsections, we will briefly talk about the first two categories followed by the rational in choosing the right approach with our problem in hand.

3.1. First order reliability method

In this section, a basic introduction to the conventional First Order Reliability Method (FORM) along with its formulation is given. This method is restricted to normal random parametric space. So, all the input random parameters x_i should be transformed to its reduced version having a standard normal Gaussian distribution. This step is done so as to simplify the integrand $f_X(\mathbf{x})$ in Eq. (27) so that its contours on the random parameter space will be more regular and symmetric. Assuming that all the n input random parameters in X space follows a Gaussian distribution $\mathscr{N}(\mu_i, \sigma_i^2)$, $i = 1, 2, \cdots, n$, where μ_i and σ_i^2 are the mean and variance of the i^{th} input random parameter, they can be transformed to a standard normal distribution space $\mathscr{Y} := \mathscr{N}(0, 1)$ using a linear transformation rule as given below:

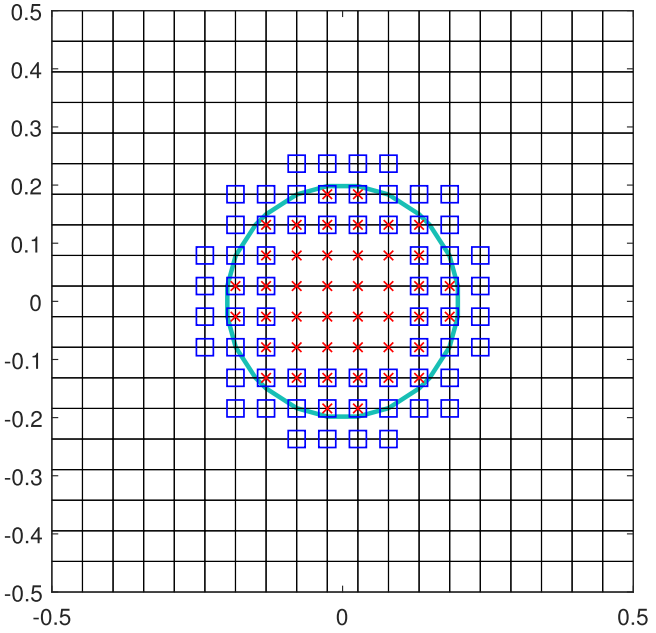

Fig. 3. Mesh for a square plate of dimensions 1 × 1m with a circular cutout of radius 0.2m, marked with blue line. Enriched nodes associated with the elements containing the cutout boundary are shown in blue squares □, while constrained nodes that lie within the cutout are marked as ∗.

Table 1
Integration rules for enriched and non-enriched elements in the presence of a cutout.

Element Type	Gaußpoints
Non-enriched element	4
Split element	3 per triangle
Split blending element	4

$$z_i = \frac{x_i - \mu_i}{\sigma_i}, \qquad i = 1, 2, \cdots, n \tag{28}$$

After the transformation, the failure probability integration becomes

$$P_f = P\Big(g(\mathbf{z}) < 0\Big) = \int_{g(\mathbf{z})<0} \phi_{\mathscr{Z}}(\mathbf{z})\mathrm{d}\mathbf{z} \tag{29}$$

where $\phi_{\mathscr{Z}}(\mathbf{z})$ is the joint pdf of all input parameters in standard normal space. Once the transformation is done, the next step is to approximate the integration boundary $g(\mathbf{z}) = 0$. FORM is based on the first order Taylor series expansion of the integration boundary as shown below:

$$g(\mathbf{z}) \approx g(\mathbf{z}^*) + \nabla g(\mathbf{z}^*)(\mathbf{z} - \mathbf{z}^*)^T \tag{30}$$

where $\mathbf{z}^*$ is the expansion point and $\nabla g(\mathbf{z}^*)$ is the gradient of $g(\mathbf{z})$ at $\mathbf{z}^*$, defined as

$$\nabla g(\mathbf{z}^*) = \left(\frac{\partial g(\mathbf{z})}{\partial z_1}, \frac{\partial g(\mathbf{z})}{\partial z_2}, \cdots, \frac{\partial g(\mathbf{z})}{\partial z_n}\right)\Big|_{\mathbf{z}^*} \tag{31}$$

The point on $g(\mathbf{z}) = 0$ that has the highest joint probability density is termed as the Most Probable failure Point (MPP). In other words, maximizing the joint pdf $\phi_{\mathscr{Z}}(\mathbf{z})$ along the limit state function $g(\mathbf{z}) = 0$ gives the location of MPP. The above statement can be mathematically formulated as follows:

$$\max_{\mathbf{z}} \prod_{i=1}^{n} \frac{1}{\sqrt{2\pi}} \exp\left(-\frac{1}{2} z_i^2\right), \quad \text{s. t.} \quad g(\mathbf{z}) = 0 \tag{32}$$

Since the function to be maximized is equivalent to minimizing $\sum_{i=1}^{n} z_i^2$, the model for the MPP (Eq. (32)) can be re-written as follows:

$$\min_{\mathbf{z}} \left\|\mathbf{z}\right\|, \quad \text{s. t.} \quad g(\mathbf{z}) = 0 \tag{33}$$

where $\|\cdot\|$ stands for the norm of a vector. The solution to the optimization problem given in Eq. (33) is the MPP and its denoted by $\mathbf{z}^* = (z_1^*, \cdots, z_n^*)$. As one can see from Figure 4 for a bivariate case, MPP is the point along $g(z_1, z_2) = 0$ which has the shortest distance to the origin of the $\mathscr{Z}$-space. Once the MPP is computed, the reliability index can be computed as $\beta = \|\mathbf{z}^*\|$.

While the procedure to determine the MPP will be detailed in Section 3.2, further details in computing the reliability index using FORM is detailed henceforth. Since at MPP $\mathbf{z}^*$, $g(\mathbf{z}) = 0$, Eq. (30) becomes

$$L(\mathbf{z}) = \sum_{i=1}^{n} \frac{\partial g(\mathbf{z})}{\partial z_i}\Big|_{\mathbf{z}^*} \left(z_i - z_i^*\right) = a_0 + \sum_{i=1}^{n} a_i z_i \tag{34}$$

where,

$$a_0 = -\sum_{i=1}^{n} \frac{\partial g(\mathbf{z})}{\partial z_i}\Big|_{\mathbf{z}^*} z_i^*, \quad a_i = \frac{\partial g(\mathbf{z})}{\partial z_i}\Big|_{\mathbf{z}^*} \tag{35}$$

Since $L(\mathbf{z})$ is a linear function of standard normal parameters as per Eq. (34), it is also normally distributed with a mean of $\mu_L = a_0$ and standard deviation given by

$$\sigma_L = \sqrt{\sum_{i=1}^{n} a_i^2} = \sqrt{\sum_{i=1}^{n} \left(\frac{\partial g}{\partial z_i}\Big|_{z_i^*}\right)^2} \tag{36}$$

Now using these two information, the probability of failure can be computed as

$$P_f \approx P(L(\mathbf{z}) < 0) = \Phi\left(\frac{-\mu_L}{\sigma_L}\right) = \Phi\left(\frac{\sum_{i=1}^{n} \frac{\partial g}{\partial z_i}\Big|_{\mathbf{z}^*} z_i^*}{\sqrt{\sum_{i=1}^{n} \left(\frac{\partial g}{\partial z_i}\Big|_{\mathbf{z}^*}\right)^2}}\right) = \Phi\left(\sum_{i=1}^{n} \alpha_i z_i^*\right) \tag{37}$$

where

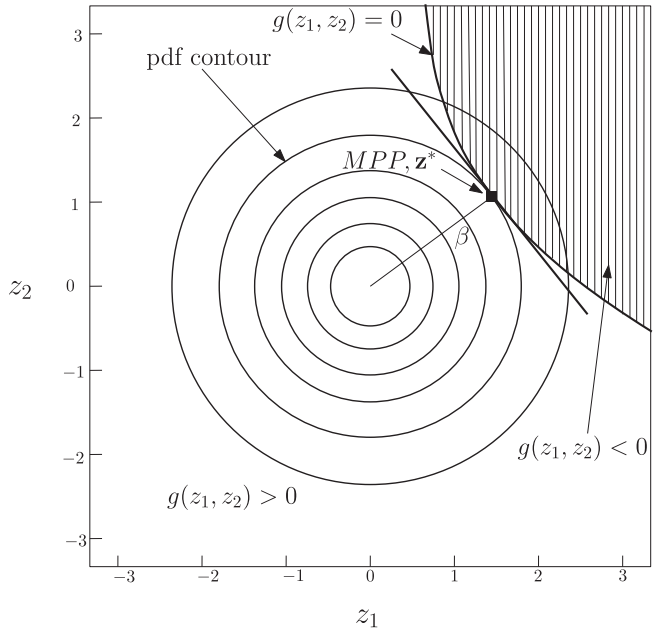

Fig. 4. Probability integration using FORM.

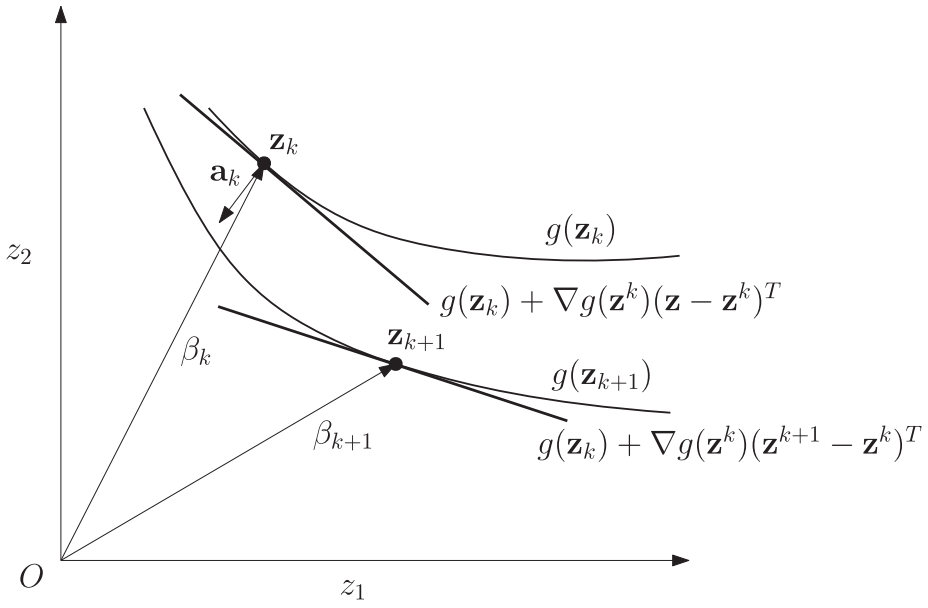

Fig. 5. Schematic representation of a MPP Search.

$$\alpha_i = \frac{\left.\frac{\partial g}{\partial z_i}\right|_{\mathbf{z}^*}}{\sqrt{\sum_{i=1}^{n}\left(\left.\frac{\partial g}{\partial z_i}\right|_{\mathbf{z}^*}\right)^2}} \tag{38}$$

Let the collection of vectors α_i be represented as follows

$$\mathbf{a} = \left(\alpha_1, \alpha_2, \cdots, \alpha_n\right) = \frac{\nabla g(\mathbf{z}^*)}{\|\nabla g(\mathbf{z}^*)\|} \tag{39}$$

The probability of failure can be finally written in the following format:

$$P_f \approx \Phi\left(\sum_{i=1}^{n} \alpha_i z_i^*\right) = \Phi(\mathbf{a}\mathbf{z}^{*T}) \tag{40}$$

The MPP $\mathbf{z}^*$, reliability index $\beta = \|\mathbf{z}^*\|$ and the direction of gradient at MPP, $\mathbf{a}$ are therefore related to each other as

$$\frac{\mathbf{z}^*}{\beta} = -\mathbf{a} \tag{41}$$

Substituting Eq. (41) in Eq. (40), results in

$$P_f \approx P\left(L(\mathbf{z}) < 0\right) = \Phi\left(\mathbf{a}\mathbf{z}^{*T}\right) = \Phi\left(-\beta\mathbf{a}\mathbf{a}^T\right) = \Phi\left(-\beta\right) \tag{42}$$

Finally, the reliability of the system is given by

$$R = 1 - P_f = 1 - \Phi(-\beta) = \Phi(\beta) \tag{43}$$

3.2. Search for MPP

Before proceeding with FORM/SORM, it has been made clear in Section 3.1 that it is key to locate the MPP in the standard normal space. In this section, the commonly used MPP search algorithm will be discussed. The search is based on a recursive formula and on the linearization of the performance function, as highlighted in Figure 5 and explained below.

Let MPP in the k'th iteration be $\mathbf{z}^k$. The performance function is expressed in a linearized form at $\mathbf{z}^k$ as shown by the lower line in Figure 5.

$$g(\mathbf{z}) = g(\mathbf{z}^k) + \nabla g(\mathbf{z}^k)(\mathbf{z} - \mathbf{z}^k)^T \tag{44}$$

Letting the linearized function to be zero, then the MPP $\mathbf{z}^{k+1}$ in the next iteration should be on the line as

$$g(\mathbf{z}^{k+1}) = g(\mathbf{z}^k) + \nabla g(\mathbf{z}^k)(\mathbf{z}^{k+1} - \mathbf{z}^k)^T = 0 \tag{45}$$

From Eq. (40),

$$\begin{aligned} \mathbf{z}^k &= -\beta^k\mathbf{a}^k \\ \mathbf{z}^{k+1} &= -\beta^{k+1}\mathbf{a}^k \end{aligned} \tag{46}$$

Upon substituting Eq. (46) into Eq. (45), one gets the followings:

$$\begin{aligned} & g(\mathbf{z}^k) + \nabla g(\mathbf{z}^k)(\mathbf{a}^k)^T(\beta^k - \beta^{k+1}) = g(\mathbf{z}^k) + \|\nabla g(\mathbf{z}^k)\|(\beta^k - \beta^{k+1}) = 0 \\ & \beta^{k+1} = \beta^k + \frac{g(\mathbf{z}^k)}{\|\nabla g(\mathbf{z}^k)\|} \\ & \mathbf{z}^{k+1} = -\mathbf{a}^k\left(\beta^k + \frac{g(\mathbf{z}^k)}{\|\nabla g(\mathbf{z}^k)\|}\right) \end{aligned} \tag{47}$$

The last equation in Eq. (47) gives the recursive formula in estimating the MPP. As a starting point for the same, $\mathbf{z}^0 = 0$ is chosen. For the stopping criterion, the absolute change in the position of the iteration points is checked against a user defined criteria: $\|\mathbf{z}^{k+1} - \mathbf{z}^k\| \leqslant \epsilon$.

3.3. Second Order Reliability Method

The conventional Second Order Reliability Method (SORM) is based on second-order Taylor series approximation of the nonlinear limit state function so as to better approximate its curvature. The expansion about the MPP $\mathbf{z}^*$ is:

$$g(\mathbf{z}) \approx g(\mathbf{z}^*) + \nabla g(\mathbf{z}^*)(\mathbf{z} - \mathbf{z}^*)^T + \frac{1}{2}\left(\mathbf{z} - \mathbf{z}^*\right)\mathbf{H}(\mathbf{z}^*)(\mathbf{z} - \mathbf{z}^*)^T \tag{48}$$

where $\mathbf{H}(\mathbf{z}^*)$ is the Hessian matrix evaluated at MPP:

$$\mathbf{H}(\mathbf{z}^*) = \begin{bmatrix} \left.\frac{\partial^2 g}{\partial z_1^2}\right|_{\mathbf{z}^*} & \left.\frac{\partial^2 g}{\partial z_1 z_2}\right|_{\mathbf{z}^*} & \cdots & \left.\frac{\partial^2 g}{\partial z_1 z_n}\right|_{\mathbf{z}^*} \\ \left.\frac{\partial^2 g}{\partial z_2 z_1}\right|_{\mathbf{z}^*} & \left.\frac{\partial^2 g}{\partial z_2^2}\right|_{\mathbf{z}^*} & \cdots & \left.\frac{\partial^2 g}{\partial z_2 z_n}\right|_{\mathbf{z}^*} \\ \vdots & \vdots & \ddots & \vdots \\ \left.\frac{\partial^2 g}{\partial z_n z_1}\right|_{\mathbf{z}^*} & \left.\frac{\partial^2 g}{\partial z_n z_2}\right|_{\mathbf{z}^*} & \cdots & \left.\frac{\partial^2 g}{\partial z_n^2}\right|_{\mathbf{z}^*} \end{bmatrix} \tag{49}$$

A simple closed-form solution for the failure probability computation is derived using the theory of asymptotic approximation in [41] as:

$$P_f = \Phi\left(-\beta\right)\prod_{i=1}^{n-1}(1+\beta\kappa_i)^{-0.5} \tag{50}$$

where β is the reliability index obtained using FORM and κ_i are the principal curvatures of the limit state at MPP. The procedure to obtain the first $(n-1)$ curvatures is detailed next. First, the standard Gaussian random parameters $\mathbf{z}$ are rotated to another set of coordinates, $\mathbf{v}$, in such a way that the last component of the new set v_n, coincides with the α measure, which is the unit gradient vector of the limit state at the design point (see Figure 6 for the case of 2 random parameters). This orthogonal transformation can be written as:

$$\mathbf{v} = \mathbf{R}\mathbf{z} \tag{51}$$

where $\mathbf{R}$ is the rotation matrix. For the case of just 2 random parameters, the rotation matrix will be

$$\mathbf{R} = \begin{bmatrix} cos(\theta) & sin(\theta) \\ -sin(\theta) & cos(\theta) \end{bmatrix} \tag{52}$$

where θ is the rotation angle about the origin of the random space, as highlighted in Figure 6.

For the case of more than 2 random parameters, the transformation matrix $\mathbf{R}$ is computed in two step:

step1: Construct the $\mathbf{R}_0$ matrix as follows:

$$\mathbf{R}_0 = \begin{bmatrix} 1 & 0 & \cdots & 0 \\ 0 & 1 & \cdots & 0 \\ \vdots & \vdots & \ddots & \vdots \\ \alpha_1 & \alpha_2 & \cdots & \alpha_n \end{bmatrix} \tag{53}$$

where $\alpha_1, \alpha_2, \cdots, \alpha_n$ are the components of the unit gradient vector $\mathbf{a}$ at the design point, MPP.

step2: Once the matrix $\mathbf{R}_0$ is computed, the Gram-Schmidt orthogonalization procedure is applied to $\mathbf{R}_0$ whose rows are $\mathbf{r}_{0_1}, \mathbf{r}_{0_2}, \cdots, \mathbf{r}_{0_n}$, to get the matrix $\mathbf{R}$ whose rows are $\mathbf{r}_1, \mathbf{r}_2, \cdots, \mathbf{r}_n$. The procedure for the above may be written as follows. The n'th row of $\mathbf{R}$ is simply $\mathbf{r}_n = \mathbf{r}_{0_n}$, while the other rows are computed in a backward order using the formula given below:

$$\mathbf{r}_k = \mathbf{r}_{0_k} - \sum_{j=k+1}^{n}\left[\frac{\mathbf{r}_j\mathbf{r}_{0_k}^T}{\mathbf{r}_j\mathbf{r}_j^T}\mathbf{r}_j\right] \tag{54}$$

Once the $\mathbf{R}$ matrix is obtained, a new matrix $\mathbf{A}$, whose elements are denoted by A_{ij} is computed as follows:

$$A_{ij} = \frac{(\mathbf{R}\mathbf{H}\mathbf{R}^T)_{ij}}{|\nabla g(\mathbf{v}^*)|} \tag{55}$$

where H is the Hessian matrix evaluated at the design point. Since v_n coincides with the β-vector, the last row and column of the $\mathbf{A}$ matrix and the last row in the $\mathbf{v}$ vector are dropped. Finally the limit state function can be written using a second-order approximation in the rotated space $\mathbf{v}$ as:

$$\mathbf{Y}_n = \beta + \frac{1}{2}\mathbf{Y}^T A\mathbf{Y} \tag{56}$$

where $\mathbf{A}$ is a matrix of size $(n-1)\times(n-1)$. Moreover, the curvatures κ_i required for computing the probability of failure are just the eigenvalues of this reduced $\mathbf{A}$ matrix.

3.3.1. Limitation of conventional FORM/SORM for reliability analysis of VSCL composites with cutouts

As it can be observed from Eq. (31) and all throughout the derivation for FORM/ SORM in the earlier section, one needs to have an explicit representation of all input random parameters z_i within the definition of the limit state function $g(\mathbf{z})$. In our chosen particular problem for reliability analysis of composite plates with cutouts and including uncertainty in geometric parameters like the ply thickness, it becomes unmistakably clear that the conventional approach with FORM/SORM is not the one to be advocated for this particular application. For example, by looking at Eq. (6), one can clearly infer that, in case of random ply thickness, the integral limits become random, which makes the process of deriving an explicit representation of limit state function, $g(\mathbf{z})$ to be nearly intractable. All the more, by looking at Figure 3, it is would be impractical to derive the gradient of the limit state function w.r.t the limit state function whose zero values defines the cutout contour. Hence, there exists a clear need to come up with a surrogate model that approximates the limit state function, whose discussion will be taken up in the following section.

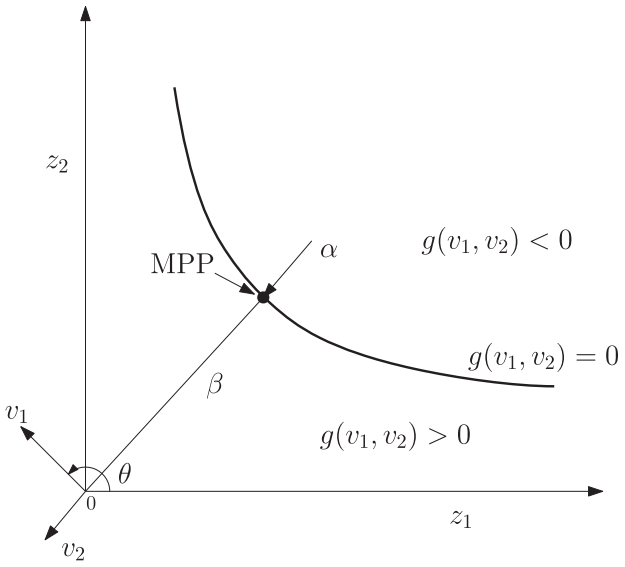

Fig. 6. Rotation of coordinates for SORM.

4. ANN based surrogate model for SRA

In the earlier section, we had highlighted the need for surrogate modelling of limit state function for the problem in hand. Some of the most commonly used surrogate models for SRA are the Response Surface Method (RSM), Kriging [42–44], Moment method, Neural Network based SRA, to name a few.

A seminal work in applying Artificial Neural Networks (ANN) in SRA was by Deng et al. [27]. For structural reliability analysis purposes, the two most commonly used ANN architectures are - multi-layer network and radial basis functions (RBF) [45]. The reader may refer to the works of Hurtadoet al. [24] for an extensive state of the art discussion on general application of neural networks in stochastic mechanics. Once an adequate surrogate model is defined between the random input parameters and its corresponding stochastic output using ANN, it is necessary to define a methodology wherein the probability of failure, P_f, can be computed using this ANN approximated meta-model. One methodology is to run an ANN-based Monte Carlo simulations for computing P_f, wherein only a finite number of finite element calculations are required for building the data set needed for ANN training process. Gradient-based methods like ANN coupled with FORM/SORM are found to abate the convergence issues normally encountered in conventional FORM/SORM (c.f. Section 3), especially when dealing with highly non-linear limit state function.

In Section 4.1, the reader is introduced to the basics of a neural network architecture, followed by the procedure to derive the first and second order derivative of limit state function w.r.t each of the input

random parameters.

4.1. Overview of an artificial neural network

In an Artificial Neural Network (ANN), each layer containing neurons gets connected to the next layer. Figure 7 shows a schematic representation of a feedforward neural network with a two-layer perceptron. As it can be seen from the outline sketch, a neuron in an ANN is considered to be a processing element. For the case of Layer 1, the output z_j from the j^{th} neuron is calculated as follows: first, all its inputs from the neurons in the preceding layer x_i are multiplied with their respective connection weights w_{ji} and added up as shown below.

$$u_j = \sum_{i=1}^{I} w_{ji} x_i \tag{57}$$

Before passing this weighted sum to the activation function, a small bias b_i is added to the same. Finally, an activation function $f(\bullet)$ is needed to transform this biased weighted sum of the inputs u_j into the output signal of the j^{th} neuron in Layer 1 as shown below.

$$z_j^1 = f\left(\sum_{i=1}^{I} w_{ji} x_i + b_j^1\right) \tag{58}$$

where I is the number of neurons in the input layer. Similar computations are carried out at each neuron within each layer of a feedforward neural-network until the output gets generated at the output layer.

The optimal design of an ANN depends on a number of parameters. The setting up stage of an ANN can generally be divided into two stages: training and testing phase. ANN training phase is when the weight and biases of a user-defined ANN gets optimized/trained using a set of input–output numerically generated samples, with sufficient variation for each ANN input parameter from their respective distribution. In the testing phase, the accuracy of trained ANN in predicting the response to new unobserved data is checked for, so as to quantify the performance of a trained ANN. Several hyperparameters influence the performance of an ANN trained using back propagation. A detailed monologue for the same can be found in the works of Goodfellow et al. [46]. For the interest of the reader, a brief introduction to the same is provided below.

Train/test ratio: Typically, the ratio of training to test dataset size normally ranges between 80/20 to 95/5 [47]. In this work, a training ratio of 80/20 is chosen (meaning 80% of samples are used for training the ANN, while the rest 20% are used for testing).

Data normalization: It is a good practice to employ data normalization so as to avoid any unwanted biases towards select dimensions in the input–output space. Among several available pre-processing techniques like Min–Max, Z-score and Decimal Scaling Normalization to name a few, Min–Max normalization is used in current studies.

ANN architecture: While the number of neurons in the input and output layer of an ANN is known *a priori*, the choice of number of hidden layers and the nodes per hidden layer remains open. It has been proven by Cybenko [48] that a one-layer ANN can sufficiently approximate any nonlinear function. While we restrict ourselves to a shallow one hidden layer ANN architecture, the choice of number of neurons in the hidden layer is discussed in the numerical Section 8.

Activation function: Choosing the right neuron activation function $f(\bullet)$ in Eq. (58) is an appropriate consideration, because it directly affects how the input data gets formatted. There exists several activation functions in the literature, depending on the range of normalized input data. In this study, given that we use a Min–Max data normalization wherein the input data gets normalized to within a range of $[-1,1]$, hyperbolic tangent function is used as activation function for hidden layer neurons, while linear activation is used in the output layer neuron.

Cost function: Training a feedforward ANN is more or less an optimization problem, for which a cost function has to be defined. There exists several cost functions to choose from, of which the Mean Squared activation function is chosen in the present study. The mean squared cost function is widely used in statistics, mainly for regression problems. The weights and bias of an ANN are optimized using stochastic gradient descent algorithm [49].

With the help of a trained ANN, the expressions to compute both the First Order Derivative (FOD) and the Second Order Derivative (SOD) of the ANN derived function approximation w.r.t each of the input parameters are presented next. The detailed derivation for the same can be found elsewhere [27,50]. However, a limitation of the back-propagation algorithm is that ANNs with the same architecture and training data set, tends to give rise to different optimal solution depending on the initialization of weights and biases.

4.2. ANN derived first order derivative

The first order derivatives can be computed by using the chain rule of differentiation. With reference to the ANN architecture as in Figure 7, the derivative of the ANN output y_k w.r.t. to its input x_i can be obtained as follows, using the assumption in our study that the transfer function in the output layer is linear and that in the hidden layer is hyperbolic tangential. Referring to Eq. (58) and Figure 7, the derivative of the output y_k w.r.t the input x_i can be obtained using the chain rule of differentiation as follows:

$$\frac{\partial y_k}{\partial x_i} = \frac{\partial y_k}{\partial z_j}\frac{\partial z_j}{\partial x_i}, \qquad j = 1, \cdots, J \tag{59}$$

where J is the number of neurons in the hidden layer.

$$\frac{\partial y_k}{\partial z_j} = w_{kj} \tag{60}$$

$$\frac{\partial z_j}{\partial x_i} = w_{ji}\left(1 - z_j^2\right) \tag{61}$$

The term that multiplies the weight factor in Eq. (61) is the derivative of the activation function (hyperbolic tangential). Substituting Eq. (60) and Eq. (61) into Eq. (59), one gets the following relation for FOD:

$$\frac{\partial y_k}{\partial x_i} = \sum_{j=1}^{J} w_{kj} w_{ji}\left(1 - z_j^2\right) \tag{62}$$

4.3. ANN derived second order derivative

In a similar manner, the second order derivative of the ANN output w.r.t the random inputs can be estimated using the chain rule [27]:

$$\begin{aligned}\frac{\partial^2 y_k}{\partial x_j \partial x_{j'}} &= \frac{\partial}{\partial x_{j'}} w_{kj} w_{ji}(1 - z_j^2) = w_{kj} w_{ji}(-2z_j)\frac{\partial z_i}{\partial x_{j'}} \\ &= w_{kj} w_{ji} w_{j'}(-2z_j)(1 - z_j^2) \qquad j, j' = 1, \cdots, I\end{aligned} \tag{63}$$

5. ANN based probability of failure estimation for variable stiffness composite laminate plates

With the aid of a brief overview over feed-forward ANN architecture and its functional derivatives, the emphasis in this section is placed on defining a suitable limit state function followed by its gradient interpretation, which will later be used in ANN based FORM-SORM. In this work, a limit state function, $g(\mathbf{x})$, is defined based on the fundamental free-vibration frequency of a VSCL plate, as shown below:

$$g(\mathbf{x}) = \frac{\lambda_p(\mathbf{x})}{\lambda_r} - 1 \tag{64}$$

where $\lambda_p(\mathbf{x})$ corresponds to the random fundamental frequency

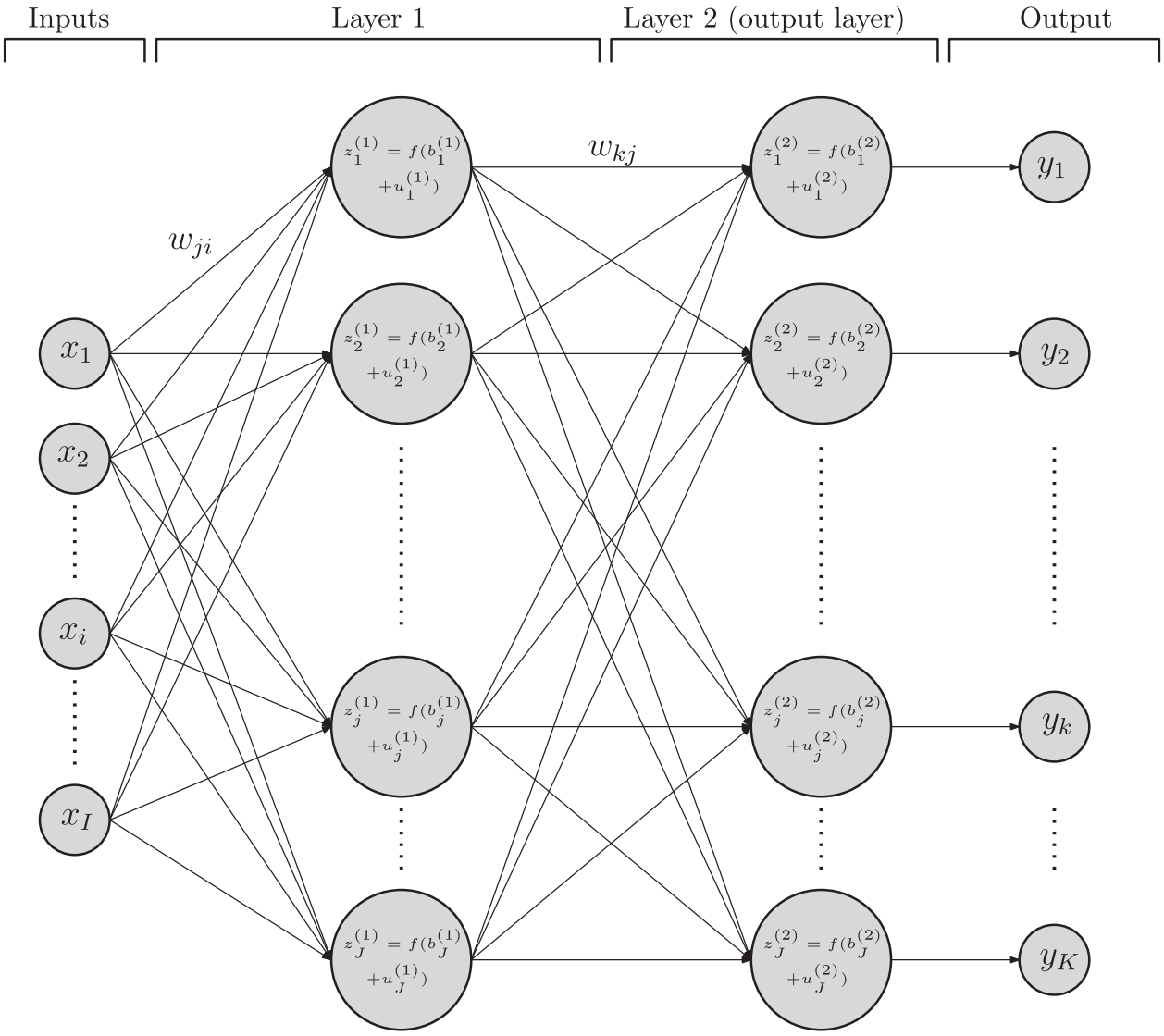

Fig. 7. Feedforward neural network with one hidden layer case.

computed for an input experimental point $\mathbf{x}$ of dimension n and λ_r stands for a user-defined critical value below which the structure is considered to be failed. Figure 8 shows a sample PDF plot of the above limit state function definition, where the probability of failure region is also highlighted.

In ANN-based FORM-SORM, partial derivatives of the performance function $g(\mathbf{x})$ w.r.t each of the input random parameters x_i, $i = 1, \cdots, n$ are required and are obtained as follows:

$$\begin{aligned}
\frac{\partial g(\mathbf{x})}{\partial x_i} &= \frac{\partial g}{\partial \lambda_p}\frac{\partial \lambda_p(\mathbf{x})}{\partial x_i} = \frac{1}{\lambda_r}\frac{\partial \lambda_p(\mathbf{x})}{\partial x_i} \approx \frac{1}{\lambda_r}\left(\frac{\partial \lambda_p(\mathbf{x})}{\partial x_i}\right)_{ANN} \qquad i = 1, 2, \cdots, n \\
\frac{\partial^2 g(\mathbf{x})}{\partial x_i \partial x_j} &= \frac{1}{\lambda_r}\frac{\partial^2 \lambda_p(\mathbf{x})}{\partial x_i \partial x_j} \approx \frac{1}{\lambda_r}\left(\frac{\partial^2 \lambda_p(\mathbf{x})}{\partial x_i \partial x_j}\right)_{ANN} \qquad i, j = 1, 2, \cdots, n
\end{aligned} \tag{65}$$

One can see from the above equation that the partial derivatives of the fundamental frequency of the system w.r.t each of the input random parameters x_i are required. The identities within the brackets $(\cdot)_{ANN}$ are the ones that we try to approximate using the trained ANN, as detailed in Section 4.2 and 4.3. Moreover, one should keep in mind that as per the definition of FORM-SORM, the derivatives of the limit state function w.r.t input parameters in their standard normal distribution space $\mathscr{Y}$ is required (c.f. Eq. (31)). However, the limit state function derivatives that are obtained using the trained ANN is based on the original input distribution of random parameters, say $\mathbf{x} \approx \mathscr{N}(\mu_i, \sigma_i^2); i = 1, \cdots, n$. Hence, a transformation as defined in Eq. (66) is required, coupled with Eq. (28).

$$\begin{aligned}
\frac{\partial g}{\partial z_i} &= \frac{\partial g}{\partial x_i}\frac{\partial x_i}{\partial z_i} \approx \left(\frac{\partial g}{\partial x_i}\right)_{ANN}\sigma_i \\
\frac{\partial^2 g}{\partial z_i \partial z_j} &\approx \left(\frac{\partial^2 g}{\partial x_i \partial x_j}\right)_{ANN}\sigma_i\sigma_j
\end{aligned} \tag{66}$$

6. Sampling method for ANN training set generation

In ANN based reliability method, the accuracy of reliability estimates is strongly dependent on the quality of the samples used to train the network [45]. The general approach adopted for generating training data set is to randomly select the samples across the whole input parameter domain and the weights and the biases of the ANN gets iteratively adjusted until a required level of accuracy is achieved in level set function approximation [51–53]. However, such traditional approach has been found to be less efficient since only a low fraction of the randomly generated samples lay in a region located close to $g(\mathbf{x}) = 0$ and that too next to the MPP.

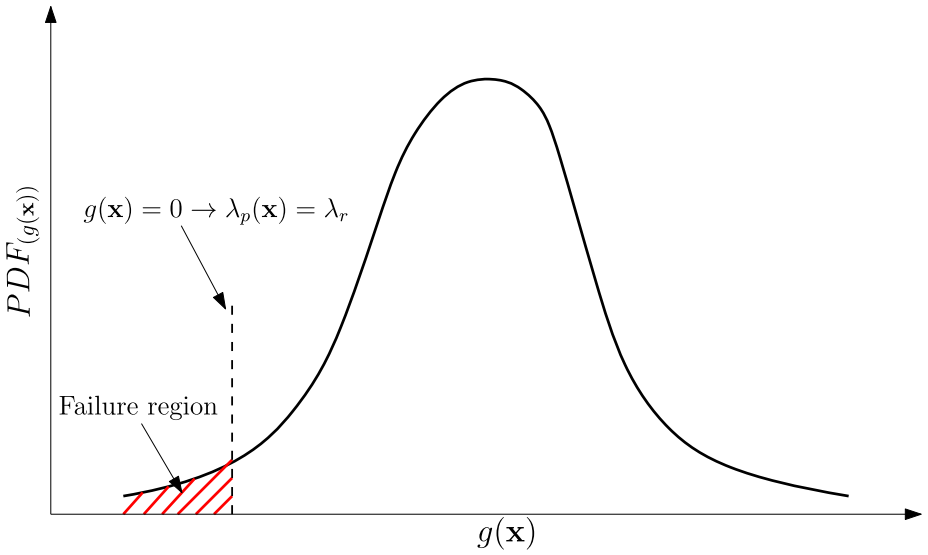

Fig. 8. Sample PDF plot of limit state function along with representation of failure region (g(**x**)<0).

6.1. Monte Carlo Simulation (MCS)

The integral in Eq. (27) can be evaluated by sampling large number of samples from the input parametric space as shown below:

$$P_{f_{MCS}} = \frac{1}{N}\sum_{i=1}^{N} \mathbb{I}\left(g(\mathbf{x}_i) < 0\right) \tag{67}$$

where $\mathbb{I}(\bullet)$ stands for the indicator function and N stands for the number of samples. The samples are chosen from the joint PDF $f_X(\mathbf{x})$. However, one of the major drawbacks of naive MCS estimator is that they tend to have an extremely high variance in P_f prediction, especially when failure probability is large only on a small fraction of samples [33]. To study the convergence of failure probability estimates as a function of number of samples, a coefficient of variation measure for Eq. (67) is used as given below [54]:

$$COV_{P_{f_{MCS}}} = \frac{\sqrt{\text{var}(P_{f_{MCS}})}}{P_{f_{MCS}}} = \sqrt{\frac{1 - P_{f_{MCS}}}{NP_{f_{MCS}}}} \approx \frac{1}{\sqrt{NP_{f_{MCS}}}} \tag{68}$$

For example, for a 10% of coefficient of variation, one would require a minimum number of sample size of $N = 10^{k+2}$ for estimating a failure probability of order 10^{-k} [55].

6.2. Importance sampling and its adaptive variants

To overcome this limitation, numerous variants have been developed, like the Subset Sampling (SS) and Importance Sampling (IS), to name a few. Importance sampling simulates from a biasing distribution that may be different from the true underlying joint distribution of input random parameters; however a correction is made for this mismatch by weighing the samples with an appropriate ratio of densities [56]. By focusing samples in regions where the integrand in Eq. (27) is large, IS can reduce the variance of a Monte Carlo estimator of an integral [57]. In short, Eq. (27) gets modified as follows:

$$P_{f_{IS}} = \int_{g(\mathbf{x})\leqslant 0} \frac{f_X(\mathbf{x})}{h_X(\mathbf{x})} h_X(\mathbf{x})\mathrm{d}x \tag{69}$$

where $h_X(\mathbf{x})$ is the bias distribution or also termed as the instrumental density. The unbiased importance sampling based P_f estimator then becomes

$$P_{f_{IS}} = \frac{1}{N}\sum_{i=1}^{N} \mathbb{I}\left(g(x_i) < 0\right)\frac{f_X(x_i)}{h_X(x_i)} \tag{70}$$

where $\{x_1, \cdots, x_N\}$ are set of samples drawn from the instrumental density $h_X(\mathbf{x})$. As per the central limit theory, the IS estimator is unbiased and and its quality can be predicted using the variance of estimation which is given below [58]:

$$Var[P_{f_{IS}}] = \frac{1}{N-1}\left(\frac{1}{N}\sum_{i=1}^{N} \mathbb{I}\left(g(x_i) < 0\right)\frac{f(x_i)^2}{h(x_i)^2} - P_{f_{IS}}^2\right) \tag{71}$$

The effectiveness of IS depends on the selection of an appropriate $h_X(\mathbf{x})$, also known as the instrumental density in literature, such that the probability sampling in Eq. (70) can be prioritized onto the region of greatest importance. Auet al. [59] proposed the concept of sampling from the instrumental density as states of a Markov chain, which asymptotically converges to the optimal instrumental sampling desnity to be represented with increase in samples. Afterwards, a kernel sampling density was constructed using these samples which was then later used as $h_X(\mathbf{x})$ in IS. Dubourg et al. [55] proposed a meta-model based importance sampling method where the meta-model to approximate the limit state function is based on the kriging approach. However, the probabilistic nature of the meta-model was used to construct a quasi-optimal $h_X(\mathbf{x})$.

7. Global reliability sensitivity analysis using artificial neural network

Apart from predicting the failure probability of a structure, it is equally important as to how to reduce the failure probability by carrying out a total sensitivity studies. Several work have been published along these lines. Broadly there exists two ways to compute the reliability based sensitivity studies, namely the Parametric Reliability Sensitivity (PRS) and Global Reliability Sensitivity (GRS). For example, Dubourg et al. [58] used the score function approach to derive the sensitivity of the failure probability w.r.t the parameter set. Assuming each of the input random parameters are Gaussian, the parameter set for the problem consists of $\theta_i = (\mu_i, \sigma_i); i = 1, \cdots, n$, where μ_i and σ_i corresponds to the mean and standard deviation of the i^{th} input random parameter. Recently, Zhang et al. [60] proposed the concept of using the principle of maximum entropy (MaxEnt) to approximate the reliability based sensitivity index using a performance function approximated using the multiplicative dimensional reduction method. Pengfei et al. proposed a method to estimate both PRS and GRS, based on importance samples obtained using quasi-optimal importance sampling passed through an Adaptive Kriging approximated performance function. However, what we are interested here is to compute the total

Table 2
Natural frequency, ω (rad/s) for a square simply supported VSCL plate without a cutout

Ref. [12]	Mesh size (Present work)			
	10 × 10	20 × 20	30 × 30	$\%\Delta_{30\times30}$
309.1	315.0	309.9	309.1	0.0136
503.3	530.5	509.3	505.9	0.5245
852.1	954.0	867.4	854.3	0.2627
1143.5	1203.4	1144.0	1134.3	0.8053
1297.3	1416.1	1324.8	1296.2	0.0805

sensitivity indices and for that, we will be using the procedure outlined in [61]. The reader is advised to refer to the work of Wei et al. [61] for the detailed derivations and procedures to be followed for both MCS based and Importance Sampling based Total Sensitivity Index estimation for each input random parameters on the structural failure probability.

8. Numerical examples

In this section, the proposed ANN based methodology for predicting the failure probability of a VSCL plate in the presence of both geometric and material uncertainties is studied. An in–house code was developed to numerically estimate the first natural mode of vibration of a VSCL plate with an explicit cutout representation using the XFEM, given a deterministic set of input parameters. The influence of various geometric parameters, viz., plate aspect ratio, a/b, ply thickness t_k, fiber orientation angle $<\Theta_0^k|\Theta_1^k>$ and the geometry of the cutout on the probability of the failure is systematically studied. The plate is assumed to be simply supported on all edges and is discretized using four noded shear flexible structured quadrilateral element with five dofs per node (u_o, v_o, w_o, β_x, β_y). All computations were carried out on a desktop with Intel Quad Core i7, 2.40 GHz CPU with 8 GB RAM.

8.1. Validation of deterministic code with literature results

Before proceeding with a systematic parametric study, the deterministic results from the present work is validated against the results in the literature for a square VSCL plate (a = b = 1 m) without cutouts. All parameters are assumed to be deterministic and the plate is made up of three layers with the following layup: [<30°, 0° > , < 45°, 90° > , < 30°, 0°>]. Total thickness of the plate is taken as 0.01 m. The material properties are: $E_1 = 173$ Gpa, $E_2 = 7.2$ GPa, $G_{12} = G_{13} = G_{23} = 3.76$ GPa, $\nu_{12} = \nu_{13} = \nu_{23} = 0.29$ and $\rho = 1540$ kg/m^3. Table 2 presents the convergence of the first five fundamental frequencies with mesh refinement. Based on a progressive refinement, a structured mesh of 30×30 is found to be adequate to model the plate.

Next, the probability of failure predicted using the ANN trained FORM/SORM method is validated with the results available in the literature for Constant Stiffness Composite Laminate (CSCL) [50] in the absence of a cutout. The plate is assumed to be a square with thickness $h = 0.1$. Table 3 summarizes the statistical distribution of all the input parameters. All units are in SI. A stacking sequence of [0°/45°/−45°/90°] is considered. A 1000 samples were generated using the statistical distribution of the input parameters given in Table 3. Out of these 1000 samples, 500 were used for training the ANN with an architecture of [11–10-1] (similar to [50]), while the remaining 500 samples were shared between testing and validation phase. Hyperbolic tangent activation function was used for the hidden layer (Logistic Sigmoid activation function was used for the hidden layer in Tawfik et al. [50]), except for the output layer where a linear activation function is used and $\omega_r/\omega_p = 0.97$ is used in this study.

Tables 4 and 5 compares the predicted *Most Probable Point* (MPP) for failure, the probability of failure P_f and the reliability index β using our in–house built MATLAB code with the results available in [50]. It is evident that a good agreement in predictions is achieved. The small

Table 3
Statistical distribution of basic random parameters used for validation of NN based FORM/SORM Matlab code validation [50].

Property	E_{11}	E_{22}	G_{12}	G_{23}	G_{13}	ν_{12}	ρ	$\Delta\theta$
Mean	16.48	1.4	0.87	0.45	0.87	0.334	1000	0°
Std Dev	0.61	0.05	0.052	0.014	0.052	0.01	36	1.8 °

Table 4
MPP for a square simply supported composite laminate with [0°/45°/−45°/90°] layup.

Random parameters	Present Work	Tawfik et al. [50]
E_{11} (GPa)	16.098	16.099
E_{22} (GPa)	1.3903	1.3828
G_{12} (GPa)	0.8556	0.8399
G_{23} (GPa)	0.4494	0.4496
G_{13} (GPa)	0.8618	0.8641
ν_{12}	0.3335	0.3337
ρ (kg/m^3)	1038	1036.6
θ_1(°)	0.543	0.258
θ_2(°)	44.928	44.525
θ_3(°)	−45.075	−45.480
θ_4(°)	90.543	90.258

Table 5
Comparison of the safety index (β) and probability of failure (P_f) for SSSS [0°/45°/−45°/90°] square laminate.

Method		β	P_f
FORM	Present Work	1.3545	0.0878
	Tawfik et al. [50]	1.3248	0.0926
SORM	Present Work	1.3519	0.0882
	Tawfik et al. [50]	1.4187	0.0780

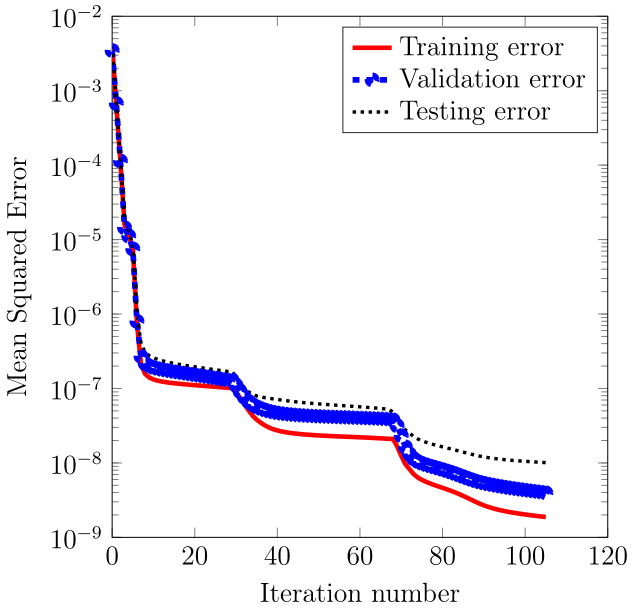

Fig. 9. Training, Validation and Testing errors of ANN. Case for the reliability estimates w.r.t the first mode of vibration studies for a SSSS [0°/45°/−45°/90°] composite plate using a [11–10-1] ANN architecture with randomness in input parameters as given in Table 3.

Table 6
Random parameters in the analysis of the limit state function w.r.t the first mode of vibration for VSCL plate with cutout.

Material uncertainties					
Sl.No.	Random parameters	Symbols	Mean Value	CoV	Distribution type
1.	Longitudinal modulus (Pa)	E_{11}	1.73e11	0.03701 [2]	LogNormal
2.	Transverse modulus (Pa)	E_{22}	7.2e9	0.03571 [2]	LogNormal
3.	In-plane shear modulus (Pa)	G_{12}	3.76e9	0.05977 [2]	LogNormal
4.	Density (kg/m^3)	ρ	1540	0.036 [2]	LogNormal
		Geometric uncertainties			
5.	Cutout major axis (m)	d	0.4	0.00025 [3]	Normal
6.	Cutout ellipticity (–)	c/d	1	0.005 [3]	Normal
7.	Cutout center location (m)	x_c	0.0	0.001 [1]	Normal
8.	Cutout center location (m)	y_c	0.0	0.001 [1]	Normal
9.	Ply thickness (m)	t^k	0.0033	0.04 [2]	LogNormal
10.	Ply angle (°)	$<\Theta_0^k \vert \Theta_1^k>$	<0°, 45°> < − 45°, −60°> <0°, 45°>	1.8^{*1}	Normal

[1] Standard deviation values are defined for zero mean valued parameters.
[2] CoV used in [50].
[3] Internal communication with an expert in composite machining.

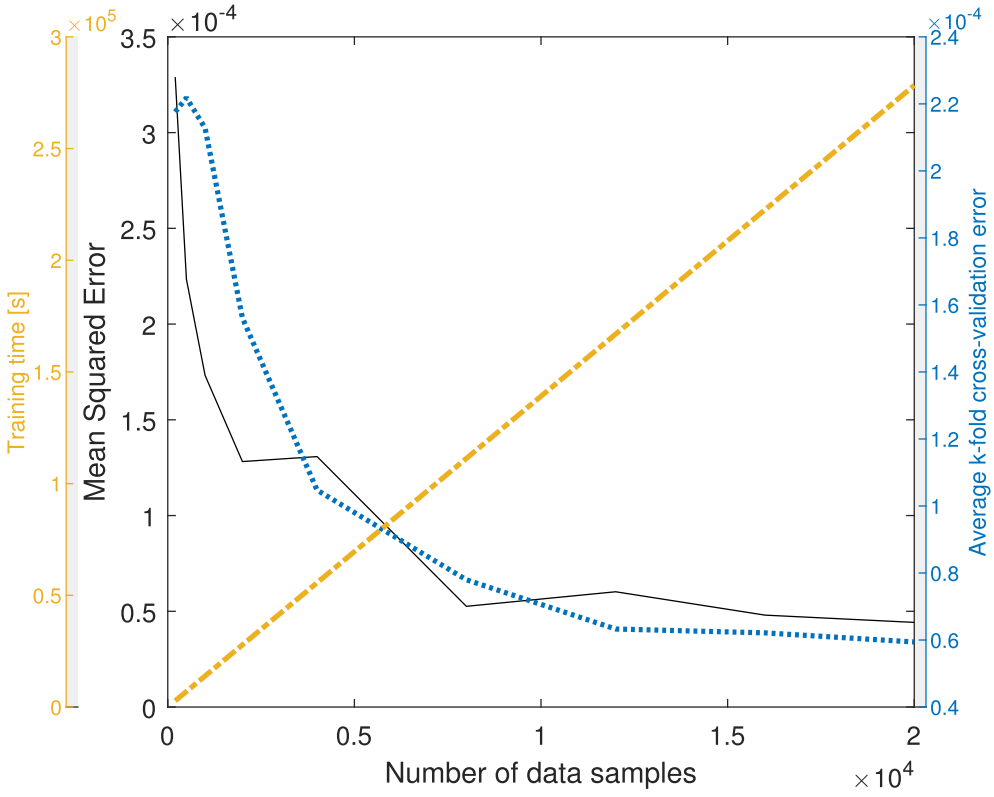

Fig. 10. Time spent on the training set preparation and ANN accuracy as function of the size of the training set.

differences in the magnitude can be attributed to: (a) the difference in the activation function selection for the hidden layer and (b) the choice of the plate deformation theory (FSDT is used in the current work, whilst, the reference work [50] is based on Third order Shear Deformation Theory (TSDT)). The training, validation and testing errors are plotted against the iteration number in Figure 9. After nearly 105 iterations, the training, validation and testing error were found to be 1.86×10^{-9}, 3.96×10^{-9} and 1.01×10^{-9} respectively.

8.2. Probability of failure and global reliability sensitivity analysis for VSCL plate with cutouts

Next, the Neural Network based probability of failure prediction using the FORM/SORM is extended to VSCL plates with cutouts. As a note to the reader, no benchmark reliability studies of Variable Stiffness Composite Laminate plates based on its fundamental frequency, existed in the literature at the time of writing this paper. To begin with, Table 6 summarizes the input parameters that are treated to be random for the case of a 3 ply VSCL composite plate (a/b = 1) along with their mean values, Coefficient of Variation (CoV) and distribution type. As it can be seen, 4 random parameters associated with material, 4 w.r.t the cutout shape, size and location and 3 w.r.t the ply angle and its thickness are considered for the reliability analysis.

A lognormal distribution is considered for all the material parameters and the ply thickness as it is not logical for them to be assigned with a negative value. Moreover, tighter control in dispersion, i.e. lower value of CoV, is assigned for geometric parameters as it would be expected in any manufacturing setting. Since the FORM-SORM formulation is based on non-correlated standard normal space, any lognormal random parameter need to be first converted to its normal space using the following relation:

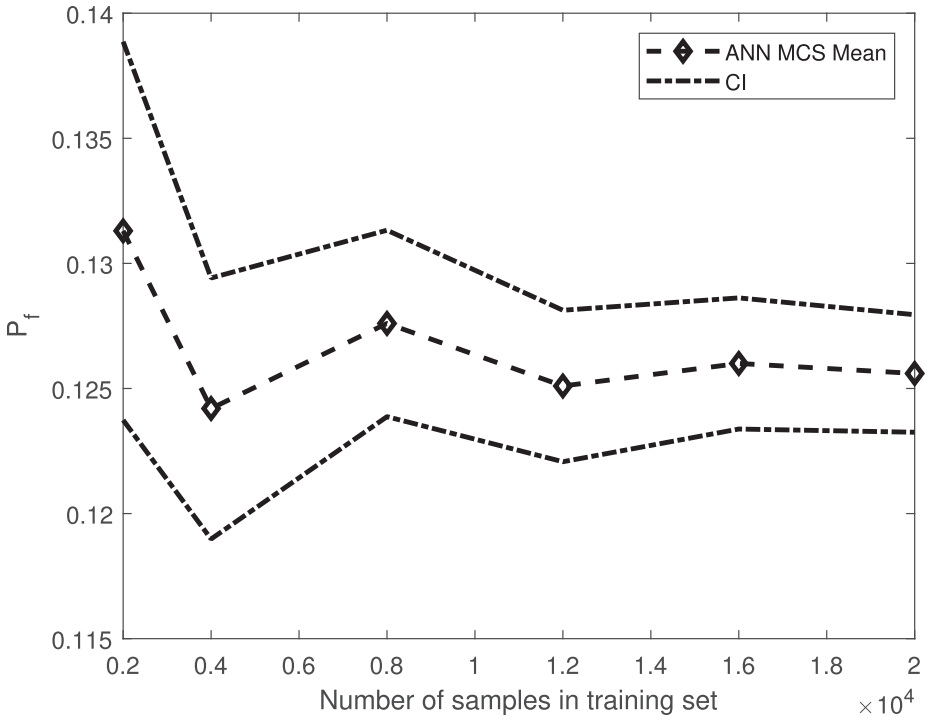

Fig. 11. Estimated probability of failure as a function of the number of elements in the training data set. CI stands for confidence interval.

$$\mu_X = 2ln(\mu_Y) - (1/2)ln(\sigma_Y^2 + \mu_Y^2)$$
$$\sigma_X^2 = -2ln(\mu_Y) + ln(\sigma_Y^2 + \mu_Y^2)$$

where subscript X and Y refers to the random parameter in the normal and lognormal space respectively, while $\mu_{(\cdot)}$ and $\sigma_{(\cdot)}$ stands for the mean and standard deviation.

For the user defined set frequency in Eq. (64), a value of $\lambda_r = 0.97\lambda_{mean}$ is chosen, where λ_{mean} is the deterministic value of first frequency mode of the VSCL plate computed using the mean value for all parameters and plate geometries.

8.2.1. ANN based reliability analysis by Monte Carlo simulation

One of the first approaches in using the ANN for reliability estimation is in approximating the Limit State Function (LSF), followed by MCS for reliability assessment. We consider data sets of different sample sizes, ranging from 2000 to 20000 samples, so as to check their influence on the capacity of ANN in approximating the LSF and the reliability analysis error. The training samples are generated using Latin Hypercube Sampling (LHS). Figure 10 plots the mean square error in ANN approximation of limit state function, total computational time involved in generating the samples and training the ANN metamodel and the average k-fold cross-validation error ($k = 10$), against the sample size.

It can be observed that the error in the network approximation for LSF approaches to zero with increasing number of samples in the input data set. However, larger the data set, more computational time is required for generating those samples. Moreover, looking at the decay trend of the average k-fold cross-validation error ($k = 10$) against the sample size, one can observe no further improvement in model generalization for sample size beyond 10, 000. Hence, to perform the ANN based reliability studies using MCS, we choose the ANN trained using 8000 samples, beyond which no significant improvement in ANN approximation of LSF was observed. Figure 11 plots the estimated failure probability along with the Confidence Interval (CI is defined as twice the standard deviation) (c.f. Eq. 68) as a function of number of sampling points. As one can observe, the CI turns out to be narrower as the number of samples in the training set increases, due to the effect of reducing standard error of the probability of failure estimations by MCS. From Figure 11, it can be observed that a converged failure probability prediction of 0.1251 is obtained using an ANN trained with a data set of 12000 samples, within a prediction uncertainty of 2.4%.

8.2.2. ANN based reliability analysis by Monte Carlo based Importance Sampling

One of the main drawbacks of ANN based MCS is that it's efficiency depends on the magnitude of the failure probability, meaning, smaller the failure probability, larger the number of samples required. However, this drawback of MCS based reliability can be overcome by forcing the sampling of experimental points using a different probability density function that is centered around the failure domain. This is the fundamental concept behind importance sampling, which was briefly introduced in Section 6.2. Here, we plan to implement an ANN for failure probability estimation that gets trained adaptively using samples chosen from an importance sampling density centered around the MPP estimates in each iterative FORM/SORM step. To make the steps involved more clearer to the reader, as a first step, the network with a given architecture gets trained with a much reduced sample size generated using Latin Hypercube Sampling, centered around the mean values of input parameters. We choose three different training sample set size, namely $N_{samples} = 50, 100, 200$, to train ANN in each iterations. The trained ANN in first stage is then used to find the MPP in the first iteration using FORM/SORM as detailed in Section 5. In the second step, an additional $N_{samples}$ samples in the surroundings of the previous MPP from the first iteration are generated using Latin Hypercube Sampling and added to the training sample set and the procedure gets repeated. The process gets terminated once the MPP generated at the i'th iteration within a hypercube that was centered at the MPP from the (i-1)'th iteration and with a width that equals the standard deviation of input random parameters. Once the ANN has been iteratively trained, failure probability is finally computed using the above trained ANN coupled with MCIS around the most recent MPP. Fig. 12 plots a schematic sketch of the flow diagram of the proposed adaptive ANN based MCIS. Table 7 presents the results obtained using the above approach.

In the current case, the design point was found to converge within

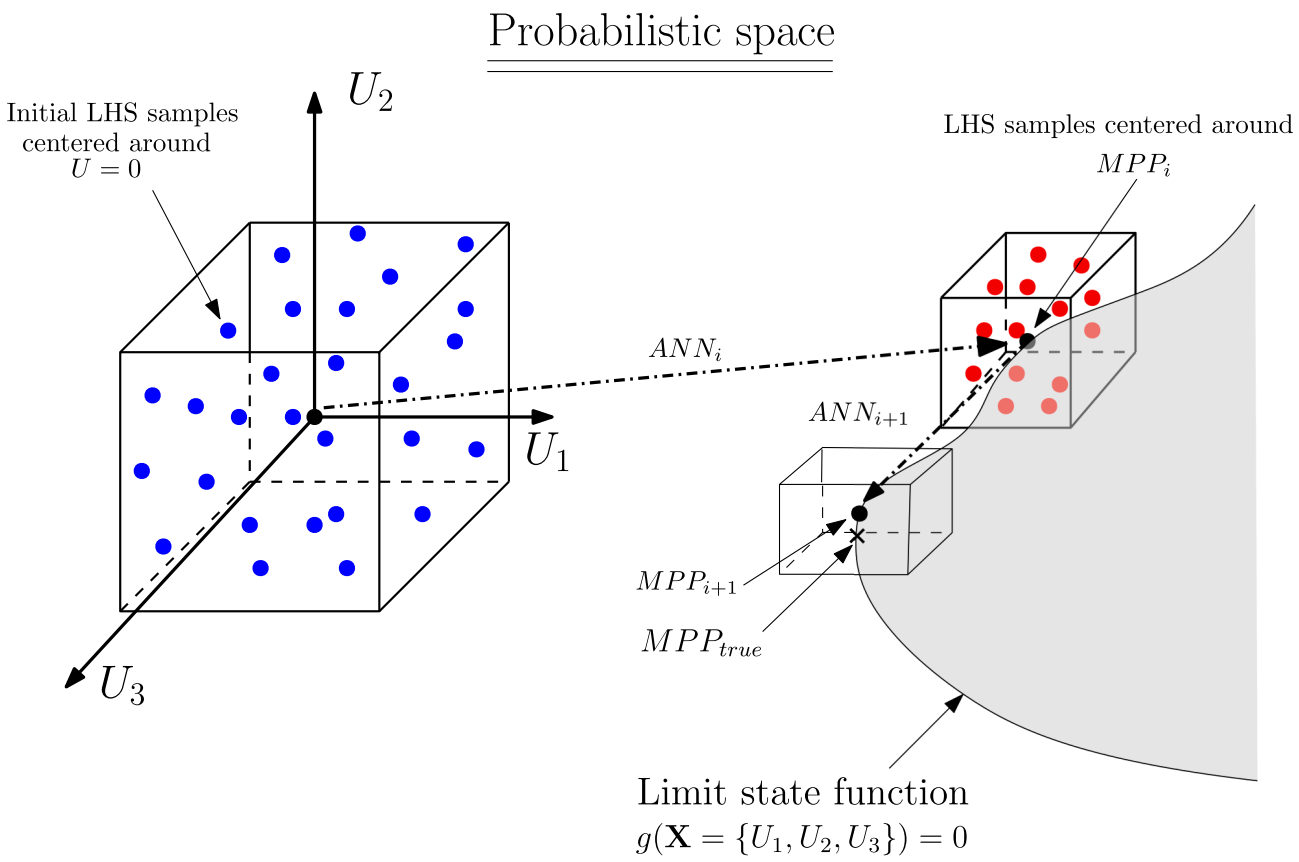

Fig. 12. Schematic sketch showing the flow diagram of the proposed Adaptive ANN based MCIS.

Table 7
Results of ANN based MCIS.

Training set (Step1 + Step2)	ANN-training		P_f (FORM/SORM + MCIS)		Total time [s]	ANN MSE
	$P_{f_{FORM}}$	$P_{f_{SORM}}$	$P_{f_{MCIS}}$	$Stddev_{P_{f_{MCIS}}}$		
50 + 50	0.0924	0.0912	0.1012	0.0016	1290	3.47×10^{-4}
100 + 100	0.1695	0.1698	0.1152	0.0013	2587	1.67×10^{-4}
200 + 200	0.1753	0.1736	0.1156	0.0013	5076	1.25×10^{-4}

the first two steps of iteration. The estimated failure probability converges to a value of $P_{f_{MCIS}} = 0.1156$ with a variance of $(0.0013)^2$ computed using Eq. (71). By adopting an adaptive ANN + MCIS approach, we see that the total computational time has been reduced to 5076 s, a reduction factor of roughly 95% when compared against the procedure adopted in Section 8.2.1.

Figure 13 plots the total sensitivity index of the failure probability to the input random parameters. In the figure, the sensitivity indices for each of the ply thickness and for the ply fibre angle orientation both at

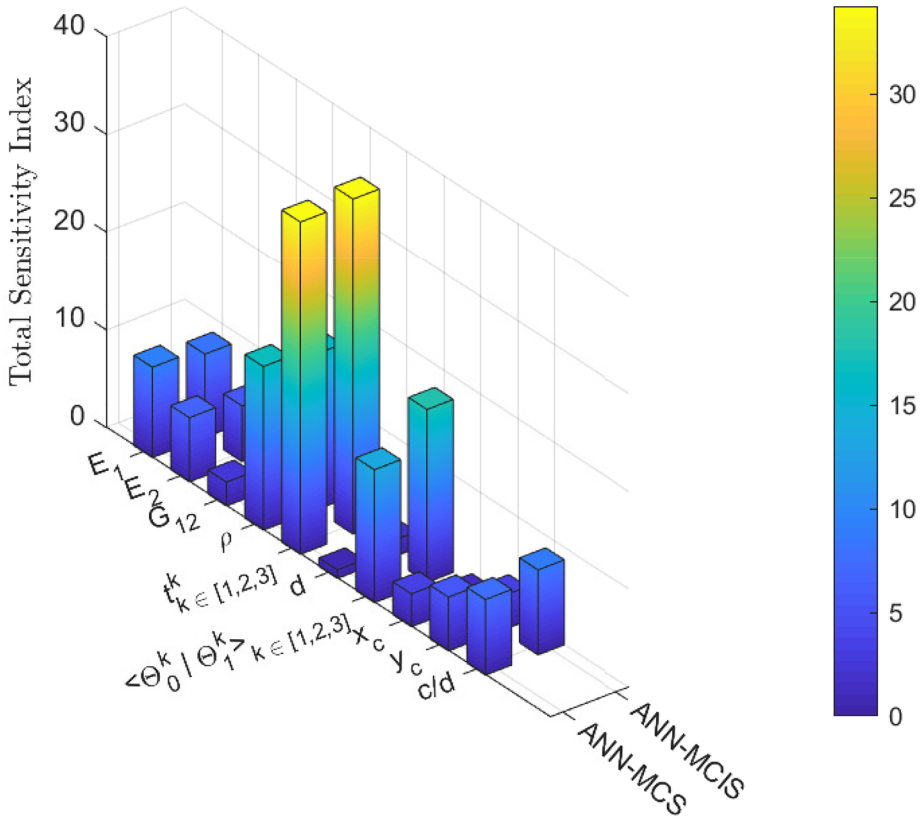

Fig. 13. Estimated total sensitivity index for each of input parameters on the failure probability of aVSCL composite plate. ANN-MCS is based on the ANN metamodel trained using 8000 samples, while ANN-MCIS is based on the metamodel obtained using the proposed adaptive importance sampling method.

Table 8
Different types of VSCL composites identified for failure probability and reliability estimates using proposed adaptive ANN-MCIS.

Composite Type	Aspect ratio (a/b)	Ply angle orientation	Remarks
Composite 1	a/b = 1	<0°, 45°> < − 45°, −60°> <0°, 45°>	Square plate with unsymmetric ply
Composite 2	a/b = 1/2	<0°, 45°> < − 45°, −60°> <0°, 45°>	Rectangular plate with unsymmetric ply
Composite 3	a/b = 1	<0°, 45°> < − 45°, −60°> < − 45°, −60°> <0°, 45°>	Square plate with symmetric ply
Composite 4	a/b = 1/2	<0°, 45°> < − 45°, −60°> < − 45°, −60°> <0°, 45°>	Rectangle plate with symmetric ply

Table 9
Results of failure probabilities of four different types of VSCL plate configurations using the proposed adaptive ANN based MCIS.

Composite Type	F_{det} [rad/s]	ANN-training		P_f (FORM/SORM + MCIS)		$P_{f_{MCS}}$
		$P_{f_{FORM}}$	$P_{f_{SORM}}$	$P_{f_{MCIS}}$	$Stddev_{P_{f_{MCIS}}}$	
1	1193.5	0.1753	0.1736	0.1156	0.0013	0.1205
2	406.08	0.1898	0.1901	0.1897	0.0016	0.1965
3	1820.4	0.1674	0.1690	0.1014	0.0012	0.1048
4	589.06	0.1842	0.1843	0.1813	0.0015	0.1880

the mid and edge locations have been coupled together, respectively. The results corresponding to ANN-MCS is obtained using the ANN metamodel trained using 8000 samples (see Section 8.2.1), while the one corresponding to ANN-MCIS are obtained using the ANN metamodel that was adaptively trained, as detailed above. One can observe that an excellent agreement is observed between both the predicted total sensitivity indices for each of the input random parameters. Moreover, the failure probability was found to be the most sensitive on upon the randomness in input ply thickness, followed by ply angle and density uncertainties.

8.2.3. Application of adaptive ANN based MCIS for failure prediction and reliability sensitivity studies for different composite plates

In this section, we extend our proposed adaptive ANN based MCIS for failure prediction and reliability estimates of four different composite plates. Table 8 summarizes four different types of VSCL composites considered for this study, with variations in aspect ratio and ply angle orientations.

Table 9 summarises the failure probabilities of the identified 4 different types of composites w.r.t the given input random parameters (c.f. Table 6). The failure probabilities were computed using the proposed adaptive ANN based MCIS, which was trained using 200 samples for each iteration.

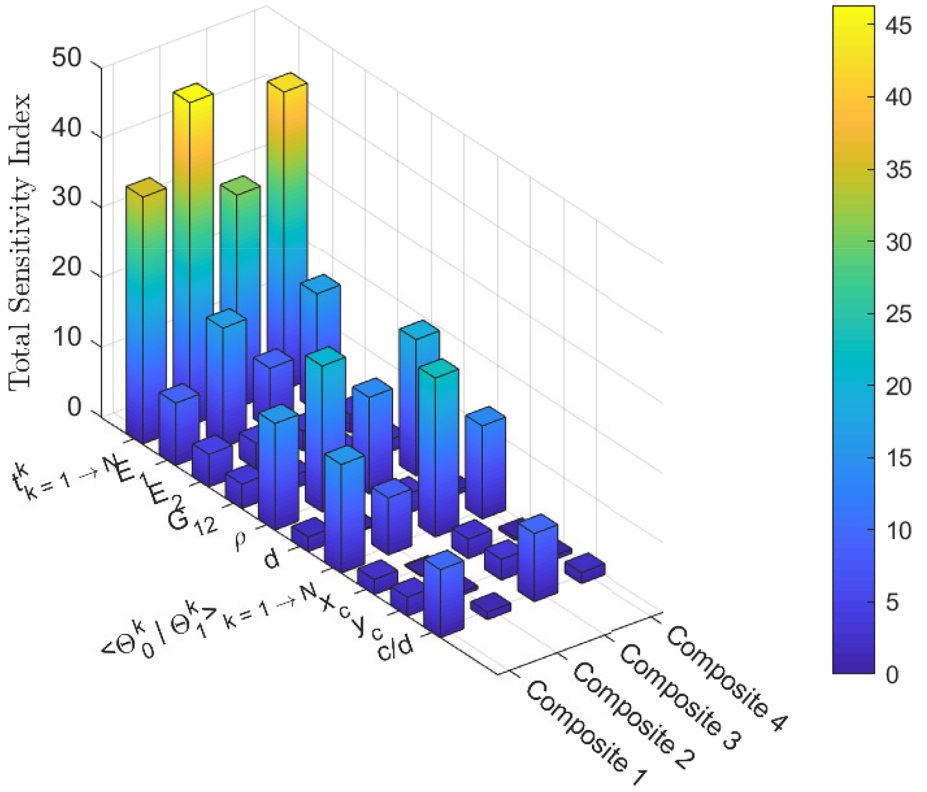

Fig. 14. Estimated total sensitivity index for each of input parameters on the failure probability for four different VSCL composite plate (c.f. Table 8).

The second column of Table 9 contains information on the deterministic fundamental frequency of respective composite types, computed at mean values of input random parameters. A value which is 97% of these deterministic values serves as λ_r in Eq. (64), which defines there respective limit-state function definition. The failure probability estimates obtained using the proposed method for the four difference composite cases, are now compared with that of MCS based failure estimates obtained using multiple finite element simulations with 10000 random samples (c.f. last column in Table 9. One can observe that a reasonable agreement is achieved between $P_{f_{MCS}}$ and $P_{f_{MCIS}}$.

Fig. 14 plots the total sensitivity index of each of the input parameters on the failure probability, for each of the four different VSCL plate configurations considered. The total sensitivity index are computed using the adaptive ANN based MCIS metamodel. From Table 9, it is clear that for a given input random parametric data, the rectangular plate with unsymmetric ply layup was found to show the maximum probability of failure, followed closely by its symmetric ply layup counterpart. Square plates, irrespective of the ply layup, was found to exhibit a lower failure probability by roughly a factor of 40%, compared to its rectangular counterpart.

Furthermore, by having a closer look at Fig. 14, we first see that the failure probability remains least sensitive to changes in certain input random parameters, irrespective of the VSCL plate configurations, namely, E_2, G_{12}, d, $x_c$and y_c (Total sensitivity index below 5%). On the other spectrum of sensitivity values, we see that the total uncertainty in ply thickness dominates in its contribution towards the failure probability, across all the 4 VSCL configurations considered. This observation matches very well with the results published in the work of Tawfik et al. [50], where the importance of taking into account the uncertainty of ply thickness on failure estimates of straight fiber composite case studies was emphasised. Moreover, changing the plate configuration from a square to a rectangular configuration was only found to exacerbate the contribution of uncertain ply thickness to the overall failure probability. However, the reverse trend was observed in the failure sensitivity w.r.t the ply angle orientation, such that for a given ply layup (un/symmetric), play angle uncertainties in square plates were found to be more sensitive to the failure probability than its rectangular counterpart.

Among the material parametric uncertainties, only E_1 and ρ was found to have a significant contribution, where the later was found to consistently exhibit greater impact on the failure probability over the former across the VSCL configurations. Finally, as far as the effect of uncertainty in hole parameters on the failure probability, its ellipticity (c/d) was found to be the most dominant of them all, especially in the case of square plates.

9. Conclusion

In this paper, both the failure probability estimates and sensitivity studies of various configurations of VSCL plates for a given set of random input parametric values has been thoroughly discussed, analyzed and its performance validated with that of conventional MCS. The geometric uncertainties in the cutout geometry was incorporated into the studies using the stochastic level set method. Aside from the conventional methods of ANN based reliability estimates for composites where randomly large number of samples are drawn from the input parametric space, our proposed method of adaptive ANN based Importance Sampling shows promise in delivering accurate results for failure predictions and total sensitivity indices, but at a cost of significant computational savings by an observed factor of nearly 95% compared to that of MCS. Moreover, the importance of having to take into account the uncertainties in ply thickness for failure probability estimates is also highlighted, irrespective of the plate aspect ratio or the ply layup sequence.

Declaration of Competing Interest

The authors declare that they have no known competing financial interests or personal relationships that could have appeared to influence the work reported in this paper.

CRediT authorship contribution statement

Tittu Varghese Mathew: Conceptualization, Methodology, Software, Writing - original draft. **P. Prajith:** Validation, Investigation, Formal analysis. **R.O. Ruiz:** Writing - review & editing. **E. Atroshchenko:** Writing - review & editing. **S. Natarajan:** Conceptualization, Methodology, Supervision, Writing - review & editing.

Appendix A. Supplementary data

Supplementary data associated with this article can be found, in the online version, athttps://doi.org/10.1016/j.compstruct.2020.112344.

References

[1] Altenbach H. Mechanics of advanced materials for lightweight structures. Proc. Inst. Mech. Eng., Part C: J. Mech. Eng. Sci. 2011;225:2481–96.
[2] Reddy JN. Mechanics of Laminated Composite Plates and Shells: Theory and Analysis. CRC Press; 2004.
[3] Gurdal Z, Olmedo R. In-plane response of laminates with spatially varying fiber orientations-variable stiffness concept. AIAA J. 1993;31:751–8.
[4] Hyer MW, Lee HH. The use of curvilinear fiber format to improve buckling resistance of composite plates with central circular holes. Compos. Struct. 1991;18:239–61.
[5] Tatting BF. Analysis and Design of Variable Stiffness Composite Cylinders Ph.D. thesis Virginia Tech; 1998.
[6] Wu KC, Gurdal Z. Variable stiffness panel structural analyses with material nonlinearity and correlation with tests. 47th AIAA/ASME/ASCE/AHS/ASC Structures, Structural Dynamics, and Materials Conference 14th AIAA/ASME/AHS Adaptive Structures Conference 7th 2006. p. 2165.
[7] Lopes C, Gürdal Z, Camanho P. Variable-stiffness composite panels: buckling and first-ply failure improvements over straight-fibre laminates. Comput. Struct. 2008;86:897–907.
[8] Setoodeh S, Gürdal Z, Watson LT. Design of variable-stiffness composite layers using cellular automata. Comput. Methods Appl. Mech. Eng. 2006;195:836–51.
[9] Senocak E, Tanriover H. Analysis of composite plates with variable stiffness using Galerkin method. Aeronaut. J. 2007;111:247–55.
[10] Cairns D, Mandell J, Scott M, Maccagnano J. Design and manufacturing considerations for ply drops in composite structures. Compos. Part B: Eng. 1999;30:523–34.
[11] Her S-C. Stress analysis of ply drop-off in composite structures. Compos. Struct. 2002;57:235–44.
[12] Ribeiro P, Akhavan H, Teter A, Warmiński J. A review on the mechanical behaviour of curvilinear fibre composite laminated panels. J. Compos. Mater. 2014;48:2761–77.
[13] Akhavan H, Ribeiro P. Natural modes of vibration of variable stiffness composite laminates with curvilinear fibers. Compos. Struct. 2011;93:3040–7.
[14] Ribeiro P, Akhavan H. Non-linear vibrations of variable stiffness composite laminated plates. Compos. Struct. 2012;94:2424–32.
[15] Loja M, Barbosa JI, Soares CM. Dynamic instability of variable stiffness composite plates. Compos. Struct. 2017;182:402–11.
[16] Venkatachari A, Natarajan S, Ganapathi M. Variable stiffness laminated composite shells–free vibration characteristics based on higher-order structural theory. Compos. Struct. 2018;188:407–14.
[17] Haldar A, Mahadevan S. Probability, Reliability, and Statistical Methods in Engineering Design. John Wiley; 2000.
[18] Sepahvand K. Spectral stochastic finite element vibration analysis of fiber-reinforced composites with random fiber orientation. Compos. Struct. 2016;145:119–28.
[19] Chen N-Z, Soares CG. Spectral stochastic finite element analysis for laminated composite plates. Comput. Methods Appl. Mech. Eng. 2008;197:4830–9.
[20] Oh D, Librescu L. Free vibration and reliability of composite cantilevers featuring uncertain properties. Reliab. Eng. Syst. Saf. 1997;56:265–72.
[21] Gosling PD, Polit O, et al. A high-fidelity first-order reliability analysis for shear deformable laminated composite plates. Compos. Struct. 2014;115:12–28.
[22] Shaker A, Abdelrahman WG, Tawfik M, Sadek E. Stochastic finite element analysis of the free vibration of laminated composite plates. Comput. Mech. 2008;41:493–501.
[23] Zhang S, Zhang L, Wang Y, Tao J, Chen X. Effect of ply level thickness uncertainty on reliability of laminated composite panels. J. Reinf. Plast. Compos. 2016;35:1387–400.
[24] Hurtado JE. Neural networks in stochastic mechanics. Arch. Comput. Methods Eng. 2001;8:303–42.
[25] Papadrakakis M, Lagaros ND, Tsompanakis Y. Structural optimization using evolution strategies and neural networks. Computer Methods Appl. Mech. Eng. 1998;156:309–33.
[26] Hurtado JE. Structural Reliability: Statistical Learning Perspectives vol. 17. Springer Science & Business Media; 2013.
[27] Deng J, Gu D, Li X, Yue ZQ. Structural reliability analysis for implicit performance functions using artificial neural network. Struct. Saf. 2005;27:25–48.
[28] Schueremans L, Van Gemert D. Benefit of splines and neural networks in simulation based structural reliability analysis. Struct.Saf. 2005;27:246–61.
[29] Nazari F, Abolbashari MH, Hosseini SM. Three dimensional natural frequency analysis of sandwich plates with functionally graded core using hybrid meshless local petrov-galerkin method and artificial neural network. Comput. Model. Eng. Sci 2015;105:271–99.
[30] Chok Y, Jaksa M, Kaggwa W, Griffiths D, Fenton G. Neural network prediction of the reliability of heterogeneous cohesive slopes. Int. J. Numer. Anal. Meth. Geomech. 2016;40:1556–69.
[31] Gomes HM, Awruch AM. Comparison of response surface and neural network with other methods for structural reliability analysis. Struct. Saf. 2004;26:49–67.
[32] Nguyen T, Kashani A, Ngo T, Bordas S. Deep neural network with high-order neuron for the prediction of foamed concrete strength. Computer-Aided Civil Infrastructure Eng. 2019;34:316–32.
[33] Lopes PAM, Gomes HM, Awruch AM. Reliability analysis of laminated composite structures using finite elements and neural networks. Compos. Struct. 2010;92:1603–13.
[34] Elhewy AH, Mesbahi E, Pu Y. Reliability analysis of structures using neural network method. Probab. Eng. Mech. 2006;21:44–53.
[35] Sohouli A, Yildiz M, Suleman A. Design optimization and reliability analysis of variable stiffness composite structures. Smart Structures and Materials. Springer; 2017. p. 245–65.
[36] Natarajan S, Baiz P, Bordas S, Rabczuk T, Kerfriden P. Natural frequencies of cracked functionally graded material plates by the extended finite element method. Compos. Struct. 2011;93:3082–92.
[37] Rajasekaran S, Murray DW. Incremental finite element matrices. J. Struct. Div. 1973;99:2423–38.
[38] Somashekar B, Prathap G, Babu CR. A field-consistent four-noded laminated anisotropic plate/shell element. Computers Struct. 1987;25:345–53.
[39] Natarajan S, Baiz P, Bordas S, Kerfriden P, Rabczuk T. Natural frequencies of cracked functionally graded material plates by the extended finite element method. Compos. Struct. 2011;93:3082–92.
[40] Aldosary M, Wang J, Li C. Structural reliability and stochastic finite element methods: state-of-the-art review and evidence-based comparison. Eng. Comput. 2018;35:2165–214.
[41] Breitung K. Asymptotic approximations for multinormal integrals. J. Eng. Mech. 1984;110:357–66.
[42] Romero V, Swiler L, Giunta A. Construction of response surfaces based on progressive-lattice-sampling experimental designs with application to uncertainty propagation. Struct. Saf. 2004;26:201–19.
[43] Kaymaz I. Application of kriging method to structural reliability problems. Struct. Saf. 2005;27:133–51.
[44] Bichon BJ, Eldred MS, Swiler LP, Mahadevan S, McFarland JM. Efficient global reliability analysis for nonlinear implicit performance functions. AIAA J. 2008;46:2459–68.
[45] Chojaczyk A, Teixeira A, Neves L, Cardoso J, Soares CG. Review and application of artificial neural networks models in reliability analysis of steel structures. Struct. Saf. 2015;52:78–89.
[46] Goodfellow I, Bengio Y, Courville A. Deep Learning. MIT Press; 2016.
[47] Gulikers T. An Integrated Machine Learning and Finite Element Framework, applied to Composite Substructure including Damage Master's thesis The Netherlands: TU Delft; 2018.
[48] Cybenko G. Approximation by superpositions of a sigmoidal function. Math. Control, Signals Syst. 1989;2:303–14.
[49] Papalambros PY, Wilde DJ. Principles of Optimal Design. New York, NY, USA: Cambridge University Press; 2003.
[50] Tawfik ME, Bishay PL, Sadek EA. Neural network-based second order reliability method (nnbsorm) for laminated composite plates in free vibration. Computer Model. Eng. Sci. 2018;115:105–29.
[51] Papadrakakis M, Papadopoulos V, Lagaros ND. Structural reliability analysis of elastic-plastic structures using neural networks and monte carlo simulation. Comput. Methods Appl. Mech. Eng. 1996;136:145–63.
[52] Anjum MF, Tasadduq I, Al-Sultan K. Response surface methodology: a neural network approach. Eur. J. Oper. Res. 1997;101:65–73.
[53] Pu Y, Mesbahi E. Application of artificial neural networks to evaluation of ultimate strength of steel panels. Eng. Struct. 2006;28:1190–6.
[54] Jian W, Zhili S, Qiang Y, Rui L. Two accuracy measures of the kriging model for structural reliability analysis. Reliab. Eng. Syst. Saf. 2017;167:494–505.
[55] Dubourg V, Sudret B. Meta-model-based importance sampling for reliability sensitivity analysis. Struct. Saf. 2014;49:27–36.
[56] Li J, Marzouk Y. Adaptive construction of surrogates for the bayesian solution of inverse problems. SIAM J. Sci. Comput. 2014;36:A1163–86.
[57] Liu JS. Monte Carlo Strategies in Scientific Computing. Springer Publishing Company; 2008. Incorporated.
[58] Dubourg V, Sudret B, Deheeger F. Metamodel-based importance sampling for structural reliability analysis. Probab. Eng. Mech. 2013;33:47–57.
[59] Au S, Beck JL. A new adaptive importance sampling scheme for reliability calculations. Struct. Saf. 1999;21:135–58.
[60] Zhang X, Liu J, Yan Y, Pandey M. An effective approach for reliability-based sensitivity analysis with the principle of maximum entropy and fractional moments. Entropy 2019;21:649.
[61] Wei P, Lu Z, Hao W, Feng J, Wang B. Efficient sampling methods for global reliability sensitivity analysis. Comput. Phys. Commun. 2012;183:1728–43.